ACS Catalysis

pubs.acs.org/acscatalysis Research Article

# Continuous Liquid-Phase Upgrading of Dihydroxyacetone to Lactic Acid over Metal Phosphate Catalysts

Giada Innocenti, Eleni Papadopoulos, Giuseppe Fornasari, Fabrizio Cavani, Andrew J. Medford, and Carsten Sievers*

Cite This: *ACS Catal.* 2020, 10, 11936−11950 Read Online

ACCESS | Metrics & More | Article Recommendations | Supporting Information

**ABSTRACT:** The performance of Brønsted- and Lewis-acidic La, Nb, and Zr phosphates (LaPO, NbPO, and ZrPO) during the aqueous phase conversion of dihydroxyacetone (DHA) to lactic acid (LA) is investigated using a fixed-bed reactor. Mass-transfer phenomena are thoroughly investigated, and the mass-transfer coefficient is deconvoluted from the intrinsic kinetic constant for each catalyst to enable the quantitative assessment of both. NbPO is found to be mass-transfer-limited. Despite this limitation, NbPO shows the highest yield of LA at 36%. The reaction over ZrPO is not transport-limited, allowing for a rigorous analysis of intrinsic kinetics. This analysis shows that the conversion of DHA into pyruvaldehyde (PVA) follows a second-order reaction mechanism *via* a dimeric intermediate, which consolidates previous reports in the literature. Additionally, a correlation between LA production and the carbon missing from the carbon balance (carbon loss) is observed. Finally, NbPO and ZrPO show stable performance up to 10 h on stream at 150 °C. After 15 h of reaction, the PVA yield increases at the expense of LA with NbPO. This is ascribed to the deactivation of the active sites necessary to produce LA, which are different from the sites that produce PVA. This hypothesis is supported by the characterization of the spent catalyst with $^{13}C$ magic-angle spinning nuclear magnetic resonance and attenuated total reflectance infrared spectroscopy.

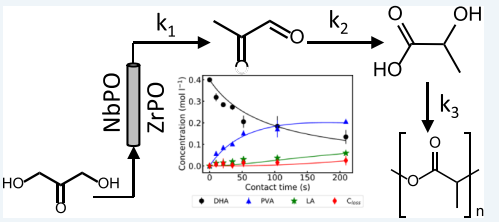


**KEYWORDS:** *mass-transfer, kinetic, second-order reaction, plug flow reactor, deactivation, pyruvaldehyde, acid catalysts*

Downloaded via Carsten Sievers on September 30, 2020 at 10:06:12 (UTC).
See https://pubs.acs.org/sharingguidelines for options on how to legitimately share published articles.

## INTRODUCTION

In the last decades, concerns regarding oil depletion and environmental issues have driven developments in biofuel production and research.[1−3] In particular, biodiesel production by triglyceride transesterification with methanol to fatty acid methyl esters exponentially increased in recent years.[4] As biodiesel production yields 10 wt % of glycerol as a by-product, there is a significant excess of the latter on the world market. The combination of glycerol supply and the limited profit margins for biofuels has motivated significant research of glycerol valorization that could help make biodiesel production economically sustainable.[5,6]

The conversion of glycerol into lactic acid (LA) is one of the most studied possible upgrading strategies.[7] LA is interesting because it can be used to produce the biopolymer poly(lactic acid) (PLA), which is widely used by the medical industry and, thanks to its biodegradability, the packaging industry.[8−11] In 2013, the global demand for LA was estimated to be 714 kilotons and is expected to reach 1960 kilotons by 2020, with a global market size of 9.8 billion USD by 2025.[12,13]

LA can be produced from glycerol through either a one-pot selective oxidation using supported metal catalysts or a two-step reaction.[7,14] In the second approach, glycerol is first converted into dihydroxyacetone (DHA) by aerobic catalytic oxidation and then further converted into LA (Figure 1).[15] The second processing step of this two-step scheme is an area of continuing investigation and the focus of this contribution.[16−20]

A study published in 1992 on the prebiotic synthesis of hexose sugars from glyceraldehyde (GLA) using Fe(OH)O reports LA as a side product.[21] However, the attention toward the conversion of trioses into LA grew after the study published in 2005 by Hayashi and Sasaki.[22] Recently, Jolimaitre *et al.*[23] proposed a kinetic model that accurately describes the homogeneously catalyzed conversion of DHA into LA and is able to distinguish the contributions of different ionic species.

The catalytic performances of Brønsted acids, such as $H_2SO_4$,[18,23,24] HCl,[18,24] and $H_3PO_4$,[18,25] were also studied. For these catalytic systems, the main product was pyruvaldehyde (PVA), with only trace amounts of LA. These results show that Brønsted acid sites can efficiently produce PVA but are not involved in LA formation. The main drawbacks of homogeneous catalysis are separation and corrosion issues, making a heterogeneous process highly desirable. The reaction mecha-

Received: August 28, 2020
Revised: September 17, 2020


© XXXX American Chemical Society

https://dx.doi.org/10.1021/acscatal.0c03761
*ACS Catal.* 2020, 10, 11936−11950

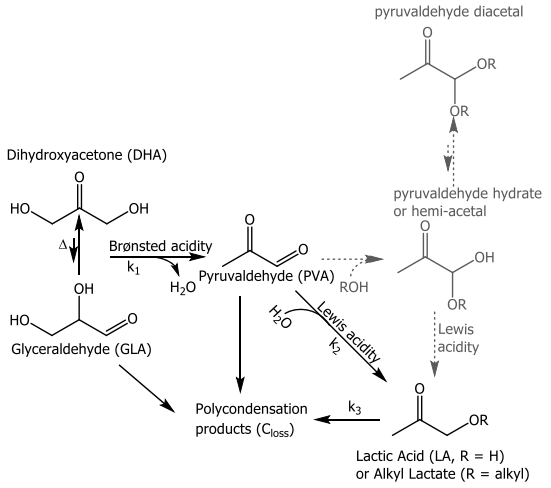


**Figure 1.** DHA upgrading mechanism into LA or alkyl lactate in aqueous (R = H, black) or alcoholic (R = alkyl, gray) solvent, respectively. The formation of polycondensation products is modeled in this work as $k_3$, whereas the DHA dehydration and the Cannizzaro reaction of PVA are modeled as $k_1$ and $k_2$, respectively.

nism hypothesized for homogeneous catalysis, as reported in Figure 1, is equally valid for heterogeneous catalysis. In fact, it is generally accepted that GLA can isomerize on Lewis acid sites to DHA, which is the more stable isomer.[23,26] Furthermore, Rasrendra *et al.*[24] found that if DHA is used as the substrate, PVA and LA are observed as products, whereas the GLA concentration is very low. On the contrary, when GLA is used as the substrate, its concentration rapidly drops in favor of DHA and PVA, and only at longer reaction times, the LA concentration starts to be significant. Triose dehydration can be catalyzed by mild Brønsted acids.[27] The dehydration can be assisted even by Lewis acid sites, but it occurs more efficiently in the presence of Brønsted acidity.[23,28,29] Finally, PVA is converted into LA or alkyl lactate over Lewis acid sites *via* the Cannizzaro reaction, and the presence of strong Brønsted acid sites leads to the formation of PVA diacetal as a side product in alcoholic solvents.[30] According to the active site requirements, the ideal heterogeneous catalyst possesses Brønsted and Lewis acid sites with a specific strength.

Commercial zeolites,[31] desilicated zeolites,[32] Ga-zeolites,[16,33] Sn-zeolites,[17,34−36] Nb-zeolites,[37] Ru-zeolites,[38] Cr−Ti/$SiO_2$,[39] Pt(dppe) supported on montmorillonite,[40] $ZrO_2$-based mixed oxide,[41] deformed orthorhombic $Nb_2O_5$,[20] Sn−$Al_2O_3$,[42] Sn−$Nb_2O_5$,[43] Sn-silica mesoporous material (MCM-41),[44,45] Sn-containing porous carbon silica material,[19] Sn−hydroxyapatite,[46] Sn−montmorillonite,[47] and modified Sn−phosphates[25,48] were proposed as catalysts. Unfortunately, zeolites and similar materials suffer from limited hydrothermal stability. For example, when USY is exposed to LA in an aqueous environment at an elevated temperature, its framework is irreversibly damaged, leading to loss of pore volume, surface area, and acidity.[28] However, when MeOH is used as a solvent, only minor damage was observed. A majority of the studies reported in the literature use alcoholic solvents producing alkyl lactates, which need to be hydrolyzed to LA to produce PLA, requiring additional conversion and separation steps.[19,37] Easy and cheap synthesis procedures were proposed for SnP-PEG2000[25] and siliceous tin phosphate catalysts,[48] as the synthesis of porous materials is often expensive and not easily scalable.[49] The main drawbacks of tin-containing catalysts for industrial applications are their scarcity and, typically, complex and lengthy synthesis procedures.[16,32,33] Recently, Wang *et al.*[50] attempted to address the problem of lengthy synthesis procedures by proposing a $SnO_2$-doped $NbOPO_4$−cetyltrimethylammonium bromide synthesized by a sol−gel method.

SnPO, along with ZrPO, is also the object of a Chinese patent application for C3 and C6 sugar conversion into LA.[51] Metal phosphates are interesting for DHA upgrading in water, thanks to their well-known water tolerance.[52] Furthermore, the use of ZrPO, NbPO, and SnPO is well documented for reactions requiring both Brønsted and Lewis acid sites, such as HMF production from sugars.[53−55] Stable performance (a small decrease in conversion at a constant yield) was shown for phosphates used in sugar conversion for up to five reuses.

However, all the studies mentioned so far were done using a batch reactor, which is less appealing for scale-up and industrial production than a flow reactor.[56] A flow reactor allows continuous production, an evident economic advantage, as it requires less scheduled downtime and can facilitate product transportation.[57,58] Even on a lab-scale, the flow reactors are more efficient for studying reaction kinetics, transport phenomena, and catalyst deactivation.[59] The increased use of continuous flow processes in academic laboratories is critical to assess catalytic reactions for biomass valorization in a way that can be extrapolated toward scale-up.

To our knowledge, only two studies dealt with DHA transformation into alkyl lactate or LA using a continuous flow setup. Mylin *et al.*[41] studied the activity of amphoteric $ZrO_2$-based mixed oxides, both in batch and continuous flow setups, using ethanol as the solvent. $ZrO_2$−$TiO_2$ in a continuous flow system yielded 90% ethyl lactate at 140 °C. DHA conversion was stable for 7 h, whereas the ethyl lactate yield decreased by 15% over this time. A comparison between the autoclave and the continuous flow results showed that the reaction under flow conditions allows for higher LA yields, but no explanation was provided for this performance enhancement. West *et al.*[60] studied the catalytic performance of H-USY-6 (FAU) zeolite in batch and continuous liquid phase setups. In the continuous liquid phase tests at 177 °C, H-USY-6 showed continuous deactivation when $H_2O$ was used as the solvent, whereas its stability in this setup increased using MeOH. The deactivation was attributed to both carbon deposition and framework degradation. A catalyst able to work in water without strong deactivation is highly desirable as water is the greenest and cheapest solvent and also allows for the direct production of LA.[52] A cheap, easily synthesizable, and water-tolerant catalytic system needs to be developed. La, Zr, and Nb phosphates are reported among the water-tolerant solid acid catalysts,[52] but their catalytic activity for DHA conversion to LA, especially in a continuous liquid flow reactor, still needs to be assessed.

In this contribution, we investigate Nb, Zr, and La phosphates for LA production from DHA using water as the solvent in a plug flow reactor (PFR). The materials are fully characterized in terms of specific surface area, porosity, and acidity. Their performances in a continuous liquid phase setup as a function of temperature, contact time, and time on stream are evaluated. The roles of mass transfer and intrinsic kinetics for these catalysts are thoroughly analyzed. Finally, the spent catalysts are characterized to obtain insight into the reasons for their deactivation.


https://dx.doi.org/10.1021/acscatal.0c03761
ACS Catal. 2020, 10, 11936−11950

## METHODS

**Catalyst Syntheses.** Three different metal phosphate catalysts (ZrPO, LaPO, and NbPO) were synthesized by coprecipitation using the methods adapted from the literature.[61−64]

LaPO was synthesized by slowly adding an aqueous 0.8 M $La(NO_3)_3{\cdot}6H_2O$ solution (130 mL) to a continuously stirred 1.2 M $H_3PO_4$ solution (130 mL). Then, the pH was adjusted to 7 using $NH_4OH$, and the precipitate was aged under ambient conditions for 2 h. This was then filtered, washed, and dried at 80 °C overnight.[61]

ZrPO synthesis followed a similar procedure. Specifically, an aqueous 1 M $ZrOCl_2{\cdot}8H_2O$ solution (64 mL) was added dropwise to a 1 M $NH_4H_2PO_4$ solution (128 mL). In this case, the pH was not adjusted before aging the precipitate, which was then filtered, washed, and dried at 80 °C overnight.[63,64]

NbPO was synthesized using hexadecyl amine as the templating agent to enhance its surface area. Following a typical procedure, 100 mL of a 0.4 M $H_3PO_4$ ethanol solution was added dropwise to 100 mL of a 0.2 M $NbCl_5$ ethanol solution. The obtained solution was vigorously stirred for 30 min. Afterward, the pH was adjusted to 2.6 with $NH_4OH$ to obtain a white precipitate. The precipitate was filtered, washed, and added to a 0.6 M hexadecyl amine solution. The new slurry was aged for 30 min while stirring, and then the pH was adjusted to 3.5 with 85% w/w $H_3PO_4$. The obtained gel was aged in a Teflon autoclave for 2 days at 65 °C. Finally, the precipitate was filtered, washed, and dried in an oven overnight.[62]

LaPO, ZrPO, and NbPO, after drying, were calcined at 550,[64] 400,[63] and 800 °C, respectively. The calcination temperature for NbPO is the minimum necessary to completely remove the templating agent. In a temperature screening, 800 °C proved to be the minimum temperature at which the catalyst was free of coke residues after burning the templating agent.

**Catalyst Characterization.** X-ray diffraction (XRD) patterns were recorded in the range of $10° < 2\theta < 80°$ with a Philips PW 1050/81 apparatus controlled by a PW1710 unit [$\lambda$ = 0.15418 nm (Cu), 40 kV, 40 mA]. The scanning rate was 0.05° $2\theta$ $s^{-1}$ and the step time was 1 s. Crystalline phases were identified using the "Search and match!" option of X'Pert HighScore Plus and the ICSD database.

Nitrogen physisorption measurements were performed at −196 °C using a Micromeritics ASAP 2020 physisorption analyzer. The catalysts were degassed at 200 °C for 4 h before measurement. Surface areas and mesopore volumes were calculated based on the BET method[65] and BJH method,[66] respectively.

Attenuated total reflectance (ATR) IR spectra of the fresh materials, without any pretreatment, were recorded at room temperature with an ALPHA-FTIR instrument at a resolution of 2 $cm^{-1}$ after 64 scans. The spectrometer was equipped with a DLaTGS and a single reflection diamond. The ATR spectra of the catalyst after the reaction were observed on a Thermo Fisher Scientific Nicolet iS10 instrument with a Smart iTR ATR sampling accessory at a resolution of 4 $cm^{-1}$ after 64 scans. The instrument was equipped with an MCT/A detector, and the accessory had a single-reflection ZnSe crystal.

$^{31}P$ and $^{13}C$ MAS NMR spectra were measured with a Bruker AVANCE III HD 300 solid spectrometer. A rotor with an outer diameter of 4 mm and a length of 16 mm was loaded with the sample. The spinning rate was 10 kHz, and the chemical shifts were referenced at 0 ppm with respect to ammonium dihydrogen phosphate and adamantane for $^{31}P$ and $^{13}C$, respectively. $^{31}P$ MAS NMR spectra were acquired using a recycle delay of 5 s. The pulse length was 1 $\mu$s, and the spectra were acquired with 256 scans with a dwell time of 2 $\mu$s. $^{13}C$-MAS NMR spectra were measured with cross-polarization to characterize the carbonaceous residues on the catalyst surface after the reaction. The spectrum was acquired as the sum of 4096 scans with a dwell time of 22 $\mu$s and a recycle time of 10 s.

The amount of carbon deposition on the catalyst surface after the reaction was evaluated using an SDT-Q600 thermogravimetric analyzer by TA Instruments. The sample after the reaction was left to dry at room temperature and pressure for 3 days. The dried sample was initially stabilized at 25 °C for 10 min in $N_2$ flow (50 mL $min^{-1}$). Afterward, the carrier was switched to air (50 mL $min^{-1}$), and the temperature was raised at 10 °C $min^{-1}$ to 800 °C. The sample remained at the highest temperature for 10 min.

The total acid site strength and concentration of the catalyst were determined by $NH_3$ temperature-programmed desorption ($NH_3$-TPD) using a Micromeritics AutoChem II 2920 system. A 50 mg powder sample was placed in a U-shaped fixed-bed reactor, preheated at 400 °C for 1 h, and cooled to 100 °C. Then, gaseous $NH_3$ was injected to saturate the sample, followed by the introduction of He as a carrier gas to purge the excess of $NH_3$. After stabilization for 1 h, the sample was heated to 700 °C at a ramping rate of 10 °C $min^{-1}$. $NH_3$ desorption profile in the temperature range of 100−700 °C was measured using a thermal conductivity detector.

Brønsted and Lewis acidity was evaluated by pyridine adsorption followed by Fourier transform infrared (FTIR) spectroscopy. The experiments were performed using a Thermo Fisher Scientific Nicolet iS10 instrument with an MCT/A detector. Each sample was loaded into a vacuum transmission cell as a self-supported wafer (diam 1.25 cm). The sample was activated at 450 °C for 1 h under a high vacuum. A background spectrum was recorded at 150 °C. Then, pyridine (0.1 mbar) was dosed for 30 min. Subsequently, the cell was evacuated for 1 h to remove the physisorbed pyridine. Temperature-programmed desorption was carried out to determine the strength of acid sites. The sample was heated to 250, 350, and 450 °C for 1 h, but each "high-temperature" spectrum was taken at 150 °C. The concentration of Lewis and Brønsted acid sites was determined using the Lambert−Beer equation

$$C_w = \frac{A_{peak}{\cdot}S}{W{\cdot}\varepsilon} \quad (1)$$

where $C_w$ ($\mu$mol $g^{-1}$), $W$ (g), $S$ ($cm^2$), and $\varepsilon$ ($cm^2$ $\mu mol^{-1}$) indicate the weight-based site concentration, sample weight, sample disk area, and the integrated molar extinction coefficient, as reported by Tamura *et al.*, respectively.[67] By integrating the peaks around 1445 and 1545 $cm^{-1}$ after exposure to each temperature, the concentrations and strengths of Lewis and Brønsted acid sites, respectively, were evaluated. The higher the temperature of pyridine desorption, the stronger is its interaction with the acid site.

The concentrations of elements from Na to U present in the samples were detected by proton-induced X-ray emission (PIXE) analysis, performed by Elemental Analysis Inc.[68]



https://dx.doi.org/10.1021/acscatal.0c03761
ACS Catal. 2020, 10, 11936−11950

Table 1. BET Surface Area ($S_{BET}$), BJH Desorption Cumulative Pore Volume ($BJH_{DPV}$), BJH Desorption Average Pore Width ($BJH_{DPW}$), and the Total Concentration of Acid Sites Determined by $NH_3$-TPD

| | | | $S_{BET}$ | $BJH_{DPV}$ | $BJH_{DPW}$ | $NH_3$-TPD | |
|---|---|---|---|---|---|---|---|
| entry | catalyst | M/P ratio | $m^2\ g^{-1}$ | $cm^3\ g^{-1}$ | nm | $\mu mol\ m^{-2}$ | $\mu mol\ g^{-1}$ |
| 1 | ZrPO | 0.31 | 122 | 0.175 | 9.48 | 5.20 | 634 |
| 2 | NbPO | 0.62 | 69 | 0.144 | 7.97 | 4.07 | 281 |
| 3 | LaPO | 0.80 | 56 | 0.177 | 14.07 | 4.80 | 269 |

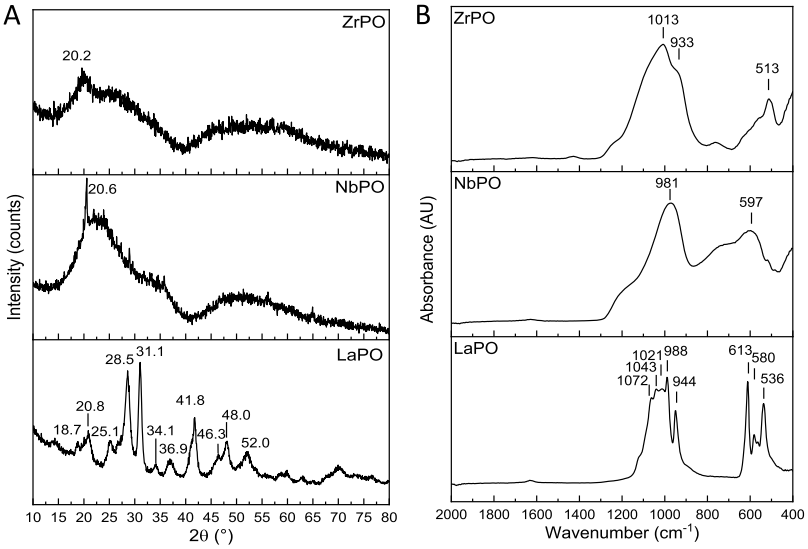


Figure 2. (A) XRD patterns for LaPO, ZrPO, and NbPO; (B) ATR−IR spectra of LaPO, ZrPO, and NbPO.

X-ray fluorescence (XRF) analysis was used to evaluate the catalyst leaching during a batch reaction at 90 °C using a Parr reactor. A PANalytical Axios Advanced dispersive wavelength spectrometer, equipped with a 4 kW power rhodium tube, was used for the analysis.

**Catalytic Reactions.** Catalytic conversion of DHA was studied in an upflow fixed-bed reactor (1/4 in. Swagelok 316 stainless steel tube). Quartz wool was used in both ends of the reactor to keep the catalyst bed in place. The reactor temperature was varied between 90 and 150 °C, and the pressure was set at 10 bar using an Equilibar EB1LF2 back-pressure regulator with a PTFE/glass diaphragm. A 0.4 M DHA aqueous solution was pumped by an Agilent 1100 Series HPLC pump at a flow rate of 0.2 mL $min^{-1}$ (except where otherwise noted). In a typical experiment, 200 mg of the catalyst (90−212 $\mu$m) was loaded, and the reaction products were collected every 30 min for 6 h with the aid of an automatic Valco selector valve. All the collected samples were filtered using a 0.45 $\mu$m polypropylene membrane before analysis. The system requires about 1.5 h to reach a steady state.

All aliquots were analyzed by high-performance liquid chromatography (HPLC) in an Agilent 1260 Infinity HPLC instrument equipped with a refractive index detector (RID). A Rezex ROA-$H^+$ column was used at 60 °C in isocratic elution mode with a 0.0025 mol $L^{-1}$ $H_2SO_4$ solution as a mobile phase at a flow rate of 0.6 mL $min^{-1}$. The RID temperature was kept at 50 °C.

The flow rate was varied (0.1−0.3 mL $min^{-1}$), and the amount of catalyst in the reactor was adjusted to maintain constant space−time to determine any external mass-transfer limitations. To evaluate potential pore diffusion limitations, the catalyst particle size was varied from 38−75 to 355−425 $\mu$m.

As the apparent density varies among the three catalysts (0.82, 0.57, and 0.38 g $mL^{-1}$ for LaPO, ZrPO, and NbPO, respectively), the space-time is expressed as follows

$$W/F = \frac{m}{\dot{V}_{tot}} \tag{2}$$

$$\tau = \frac{W/F}{\rho_a} \tag{3}$$

where $m$ (in g) is the loaded catalyst mass in the reactor, $\dot{V}_{tot}$ is the total volumetric flow in mL $s^{-1}$, and $\rho_a$ is the apparent density in g $mL^{-1}$. When the space−time is expressed as the catalyst mass-to-total volumetric flow ($W/F$) ratio, the units are g s $mL^{-1}$. The contact time ($\tau$) is obtained by dividing $W/F$ by the apparent density of the catalyst bed, and it is expressed in s. These two numbers represent how long the catalyst is in contact with the reactant with respect to the mass ($W/F$) or the volume ($W/\rho_a$) of the catalyst in the reactor. In the deactivation section, the data are reported with respect to the time on stream (in h) which, at the steady state for a PFR reactor, represents how long the reaction was carried out.

DHA conversion ($X_{DHA}$), product selectivities ($S_p$), and yields ($Y_p$) were determined using the following equations

$$X_{DHA} = \frac{C_{DHA}^{in} - C_{DHA}^{out}}{C_{DHA}^{in}} \cdot 100\% \tag{4}$$

$$Y_p = \frac{C_p^{out} \cdot z_p}{C_{DHA}^{in} \cdot z_{DHA}} \cdot 100\% \tag{5}$$

$$S_p = \frac{Y_p}{X_{DHA}} \cdot 100\% \tag{6}$$



https://dx.doi.org/10.1021/acscatal.0c03761
ACS Catal. 2020, 10, 11936−11950

where $C^{in}_{DHA}$ is the initial number of moles of DHA, $C^{out}_{DHA}$ is the final number of moles of DHA, $C^{out}_{p}$ is the number of moles of the product of interest, and $z_p$ and $z_{DHA}$ are the carbon atom numbers of the product of interest and DHA, respectively. The amount of carbon lost to the formation of deposits or undetected products was evaluated as the difference between the conversion and the sum of the yields of the detected products. For this reason, when the carbon loss was slightly negative, it was forced to zero, and the yield sum was assumed to equal the conversion. This mathematical imposition was necessary only at low temperatures (90 °C).

A detailed methodology for the kinetic analysis, the evaluation of the activation energy and the mass transfer, is reported in the Supporting Information.

## RESULTS AND DISCUSSION

**Catalyst Structure and Compositions.** The catalyst surface properties such as pore size, pore volume, and surface area were evaluated by $N_2$ physisorption. All the catalysts showed a type IV hysteresis curve, characteristic of mesoporous materials, as shown in Figure S1. LaPO presented the lowest surface area and the largest mesopore width (Table 1). On the contrary, ZrPO possessed the highest surface area, and the mesopore distribution shifted toward the micropore region, whereas NbPO showed the lowest cumulative pore volume and the smallest average mesopore width.

The composition of the catalysts was analyzed by PIXE analysis to detect all contaminants present (Table S1) and to evaluate the metal−phosphorous (M/P) ratio (Table 1).

XRD showed that NbPO and ZrPO were almost completely amorphous, whereas LaPO was semicrystalline (Figure 2A). According to the XRD patterns, the dominant crystalline phase in LaPO was $LaPO_4$ (ref 00-032-0493), as expected. This result generally agrees with the La/P ratio (0.80) of the sample. The intense diffraction at 20.56° in the X-ray diffractogram of NbPO could be assigned to the most intense diffraction of $Nb_{1.91}P_{2.82}O_{12}$ (ref 00-051-1738) or $NbPO_5$ (ref 00-019-0868). As the Nb/P ratio of 0.62 is in excellent agreement with the theoretical Nb/P ratio (0.67) of the $Nb_{1.91}P_{2.82}O_{12}$ phase, the second possibility was rejected. The broad diffraction around 20° in the X-ray diffractogram of ZrPO was in agreement with the most intense diffraction of either $Zr_2O(PO_4)_2$ (ref 00-037-0155) or $Zr(HPO_4)_2{\cdot}nH_2O$ (ref 00-019-1489). The Zr/P ratio of 0.31 obtained by PIXE analysis was in better agreement with the $Zr(HPO_4)_2{\cdot}nH_2O$ phase than with $Zr_2O(PO_4)_2$. The disagreement between the M/P ratio determined by PIXE analysis and the phases found with XRD suggests that these samples probably contain a mixture of phases.

As two of the three catalysts were predominantly amorphous, they were also studied by ATR−FTIR spectroscopy to obtain some information about their P−O bonds (Figure 2B). Broad phosphate bands (around 1000 $cm^{-1}$, P−O asymmetrical stretching vibration, and 500−600 $cm^{-1}$, $PO_4$ deformation modes) verified the amorphous character of NbPO and ZrPO. Additionally, the multiple high and sharp lines present in the LaPO ATR spectrum confirmed its semicrystallinity.[61] In fact, the strong crystal field of LaPO splits the asymmetrical P−O stretching ($\nu_3$) into four bands detectable at 1072, 1043, 1021, and 988 $cm^{-1}$ and the deformation vibration ($\nu_4$) into three peaks at 613, 580, and 536 $cm^{-1}$, respectively.[69−72] Thanks to the high LaPO crystal field, even the symmetrical stretching vibration ($\nu_1$) at 944 $cm^{-1}$ was resolved, although it should be infrared-forbidden.[71] The broad band around 750 $cm^{-1}$ in the spectra of NbPO and ZrPO is attributed to the P−O−P vibration of diphosphate groups.[73] The ZrPO band at 933 $cm^{-1}$ was already observed in the $\alpha$-zirconium hydrogen phosphate FTIR spectrum.[73] The peak position of asymmetric P−O stretching vibrations usually increases in energy with the increasing ionic radius of the cation, which is in agreement with our experimental results [Nb (215 pm) < Zr (230 pm) < La (250 pm) → 981 $cm^{-1}$ < 1013 $cm^{-1}$ < 1072 $cm^{-1}$, respectively]. The increase in the P−O vibration frequency means that the ionic character of the M−$PO_4$ bond increases as the number of $PO_4^{3-}$ moieties in the crystal cell decreases.

$^{31}$P MAS NMR spectroscopy was used to gain further information regarding phosphate species in the entire samples, including amorphous domains (Figure 3). For crystalline

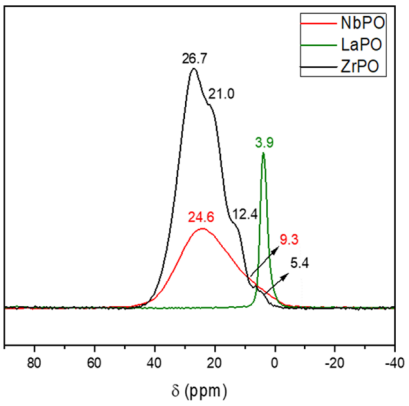


**Figure 3.** $^{31}$P-MAS NMR spectra of NbPO, LaPO, and ZrPO.

materials, the number of peaks in the $^{31}$P MAS NMR spectra for orthophosphates is equivalent to the number of non-equivalent P atoms in the catalyst structure.[74] The nomenclature for phosphate connectivity in solids depends on the number of $PO_4$ bridging oxygen, $n$. In the phosphate case, there are five possibilities from $Q^0$ (no M−O−P bond is present) to $Q^4$ (all the oxygen atoms are involved in M−O−P bonds).[75] It was possible to deconvolute the spectra of ZrPO, NbPO, and LaPO using 4, 2, and 1 Gaussian curves (Figure S2). The resonance at 4.0 ppm in the spectrum of LaPO was attributed to tetrahedral $PO_4$ connected to two La atoms ($Q^2$ topology).[74] This assignment is consistent with the monoclinic $P2_1/n$ space group characteristic for the $LaPO_4$ phase. The chemical shifts for the resonances of NbPO were 9.3 and 24.6 ppm. The peak at 24.6 ppm can be assigned to the $Q^4$ topology as it is assumed that the octahedral $NbO_6$ and the tetrahedral $PO_4$ share all the vertices. Therefore, every oxygen atom is linked to a Nb and a P atom in the $Nb_{1.61}P_{2.8}O_{12}$ phase.[76] The resonance at 9.3 ppm can be attributed to the defects that decrease the number of bridging oxygen atoms.[77] The $^{31}$P MAS NMR spectrum of ZrPO contained four signals at 26.7, 21.0, 12.4, and 5.4 ppm. In this case, it was possible to attribute the signals at 26.7, 21.0, and 12.4 ppm to $Q^4$, $Q^3$, and $Q^2$ topologies of zirconium hydrogen phosphate ($HPO_4$).[75] The peak at 9.3 ppm in the spectrum of NbPO and that at 5.4 ppm in the spectrum of ZrPO, are tentatively assigned to the $Q^2$ topology of $PO_4$. This assignment is in good agreement with the correlation between the electronegativity of the metal center and the isotropic chemical shift. In fact, by decreasing


https://dx.doi.org/10.1021/acscatal.0c03761
ACS Catal. 2020, 10, 11936−11950

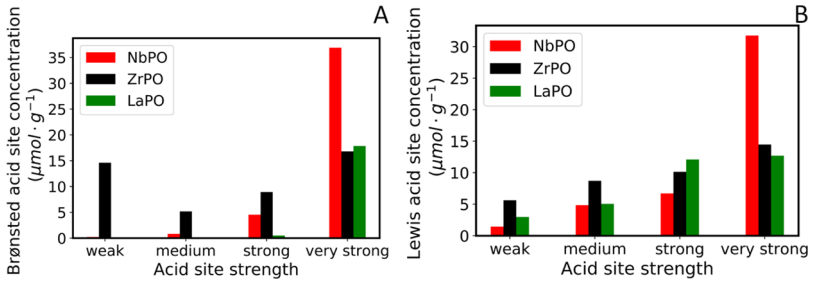


**Figure 4.** Brønsted (A) and Lewis (B) acid site concentration and strength distribution. The acid site strength is defined as weak, medium, or strong if pyridine desorbs at temperatures higher than 150, 250, or 350 °C, respectively. Sites that can retain pyridine at 450 °C are defined as very strong.

the metal electronegativity, P attracts more electron density and strengthens the P−O bond, causing an upfield shift of the chemical shift.[75] The electronegativity of Nb, Zr, and La is 1.6, 1.3, and 1.1, respectively. Moreover, in light of this result and the presence of the shoulder at 933 $cm^{-1}$ in the ATR−IR spectrum, it is suggested that the main phase of ZrPO is α-zirconium phosphate ($Zr(HPO_4)_2{\cdot}nH_2O$), which has a Zr/P ratio closer to the one obtained from the PIXE analysis (0.31). However, it is not possible to completely exclude the presence of $Zr_2O(PO_4)_2$ or another phosphate (or hydrogen phosphate) phase because of the amorphous character of this sample.

**Concentration and Strength of Acid Sites.** The acid site concentration on the catalysts was evaluated by $NH_3$-TPD. ZrPO possessed the highest acid site density (Table 1) and showed a very broad desorption peak from 100 to 450 °C (Figure S3A). It presented an absolute maximum around 180 °C and a defined shoulder centered around 290 °C. On the contrary, NbPO showed the lowest total acidity and a broad desorption profile (from 100 to 400 °C). In this case, the peak maximum is at 190 °C. The desorption curve for LaPO had a maximum centered around 160 °C. The catalysts can be placed in order, based on the density of acid sites, as follows: ZrPO > LaPO > NbPO.

NbPO contained 1 mol % of S as an impurity (Table S1) which if present as $HSO_4^-$ could contribute to the total acidity of the sample.[78] However, its concentration was 1 order of magnitude lower than that of P (10 mol %), and as a consequence, it is reasonable to assume that S contribution is less significant.

As the reaction is known to be driven by the different types of acid sites, pyridine adsorption was used to distinguish the types of acid sites and their relative strengths (Figure S3B−F). The characteristic vibrations of pyridine adsorbed on the Lewis and Brønsted acid sites were detectable at 1448 and 1540 $cm^{-1}$, respectively.[79,80]

According to a previous study, Brønsted acid sites were mostly present in the form of P−OH groups, with some contribution from M−OH groups.[61] In contrast, Lewis sites are related to coordinatively unsaturated $M^{n+}$ sites. The ratio between the concentrations of Brønsted and Lewis acid sites on phosphate catalysts is affected by the amount of chemisorbed water. In fact, a Lewis acid site can be converted into a Brønsted site by coordination or dissociative adsorption of water on unsaturated $M^{n+}$ sites.[61]

All the catalyst samples possessed both Brønsted and Lewis acidity (Figure S3E,F). LaPO showed the lowest concentration of Brønsted acid sites, but all of them were very strong (Figures S3E and 4). NbPO had the highest concentration of very strong (450 °C) Brønsted acid sites. The distribution of Brønsted acid sites in ZrPO was different; it showed the highest total concentration of Brønsted acid sites of 45 μmol $g^{-1}$ at 150 °C, but only 16 μmol $g^{-1}$ were strong enough to retain pyridine at 450 °C. LaPO has the biggest ionic radius and as a consequence the lowest number of $PO_4^{3-}$ groups in the elementary cell of $LaPO_4$. The broad distribution of Brønsted acid site strength showed by ZrPO with respect to the other two samples is in good agreement with the hydrogen phosphate structure determined by $^{31}$P-MAS-NMR. Therefore, the bigger the ionic radius, the smaller is the concentration of Brønsted acid sites in phosphate catalysts.

In contrast, for Lewis acid sites, the three catalysts showed a similar strength distribution (Figure 4B). NbPO possessed the highest number of Lewis acid sites at every desorption temperature, and there were only few weak Lewis sites. On the contrary, the Lewis acid site concentrations of ZrPO and LaPO were comparable in terms of strong and very strong acid sites, whereas ZrPO possessed a higher amount of weak and medium strength Lewis acid sites.

The total amount of Brønsted and Lewis acid sites can be ordered as ZrPO ≈ NbPO ≫ LaPO and NbPO > ZrPO > LaPO, respectively. The infrared spectroscopy results showed a decrease in the Lewis acid site concentration trend with an increasing ionic character of the M−$PO_4$ bond (NbPO < ZrPO < LaPO). The increase of Lewis acid site concentration follows an opposite trend with respect to the metal cation size. In fact, the smaller the metal ionic radius, the larger is the number of M−$PO_4$ units present in the fundamental unit cell. The distribution of phosphate groups in the unit cell is illustrated in Figure S4.

**DHA Conversion to LA.** Leaching of the metal phosphate was evaluated in a batch reactor containing 0.6 g of catalyst at 90 °C for 4 h. The substrate-to-catalyst ratio (w/w) was 1.5, and the DHA solution concentration was 0.2 M. XRF analysis of the final reaction solution detected no traces of leached metal, and the amount of phosphorus in solution was negligible (<0.008 mol %).

*Assessment of Mass-Transfer Limitations.* As mass-transfer limitations can affect reaction rates, selectivities, and even the reaction mechanism, it is critical to explicitly assess their relevance for any rigorous kinetic analysis.[81] Because of the much lower diffusivity of liquids as opposed to gasses, external transport effects are expected to be even more significant when liquid feeds are converted over solid catalysts.[59] External diffusion limitations were probed by varying the total liquid flow rate and the catalyst mass in the fixed bed by the same factor to provide a constant contact time.

External mass-transfer limitations were excluded for ZrPO because the DHA conversion did not increase when the flow


https://dx.doi.org/10.1021/acscatal.0c03761
ACS Catal. 2020, 10, 11936−11950

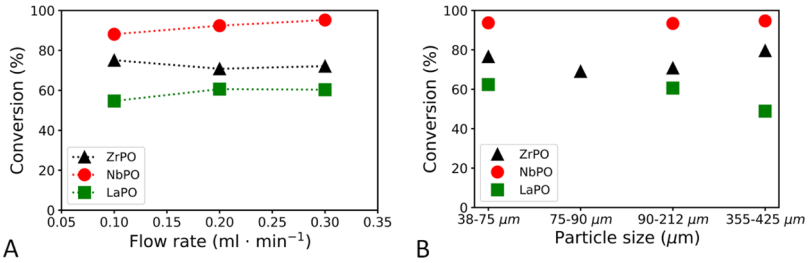


**Figure 5.** Tests for mass-transfer limitations. (A) External mass-transfer limitations. (B) Internal mass-transfer limitations. Reaction conditions: 10 bar, 60 g s mL$^{-1}$, [DHA] = 0.4 M, 150 °C for NbPO and LaPO, 130 °C for ZrPO.

**Table 2. Mass-Transfer Coefficient and Kinetic Constant Evaluated at Different Flow Rates for LaPO and NbPO, Assuming a Second-Order Kinetics**[a]

| | | NbPO | | | | LaPO | | | |
|---|---|---|---|---|---|---|---|---|---|
| $\dot{V}$ (mL min$^{-1}$) | $v$ (cm min$^{-1}$) | $k_{obs}$ (L mol$^{-1}$ s$^{-1}$) | $k_c$ (s$^{-1}$) | $k_s$ (L mol$^{-1}$ s$^{-1}$) | $k_sC_{a0}$ (s$^{-1}$) | $k_{obs}$ (L mol$^{-1}$ s$^{-1}$) | $k_c$ (s$^{-1}$) | $k_s$ (L mol$^{-1}$ s$^{-1}$) | $k_sC_{a0}$ (s$^{-1}$) |
| 0.1 | 0.43 | 0.12 | 0.0117 ± 0.002 | 2 ± 1 | 0.68 | 0.041 | 0.04 ± 0.04 | 0.09 ± 0.02 | 0.04 |
| 0.2 | 0.85 | 0.20 | 0.0234 ± 0.004 | | | 0.053 | 0.08 ± 0.08 | | |
| 0.3 | 1.28 | 0.31 | 0.0351 ± 0.006 | | | 0.053 | 0.1 ± 0.1 | | |

[a]Reaction conditions: 150 °C, 10 bar, 100−300 mg catalyst, [DHA] = 0.4 M. The errors related with $k_c$ and $k_s$ were evaluated by the addition of Gaussian noise and iterating the fit.

**Table 3. Catalytic Performance of NbPO, ZrPO, and LaPO**[a]

| | $T$ (°C) | $X_{DHA}$ (%) | $Y_{GLA}$ (%) | $Y_{PVA}$ (%) | $Y_{LA}$ (%) | $Y_{others}$ (%) | $C_{loss}$ (%) | $k_{obs}$ (L s$^{-1}$ mol$^{-1}$) | $r_a$ (mol L$^{-1}$ s$^{-1}$) |
|---|---|---|---|---|---|---|---|---|---|
| NbPO | 90 | 38 | 1 | 35 | 2 | 2 | 0 | $9.2 \times 10^{-3}$ | $6.0 \times 10^{-4}$ |
| | 110 | 61 | 1 | 52 | 5 | 2 | 1 | $2.4 \times 10^{-2}$ | $6.0 \times 10^{-4}$ |
| | 130 | 77 | 1 | 55 | 13 | 2 | 6 | $5.5 \times 10^{-2}$ | $4.5 \times 10^{-4}$ |
| | 150 | 90(±0.6) | 1(±0.6) | 27(±6) | 42(±8) | 2(±2) | 20(±4) | $1.5 \times 10^{-2}$ | $2.2 \times 10^{-4}$ |
| ZrPO | 90 | 29 | 1 | 19 | 3 | 2 | 4 | $9.7 \times 10^{-3}$ | $7.9 \times 10^{-4}$ |
| | 110 | 44(±2) | 1(±0.2) | 36(±0.6) | 5(±1) | 1(±1) | 1(±0.1) | $1.5 \times 10^{-2}$ | $7.9 \times 10^{-4}$ |
| | 130 | 71(±0.3)* | 1(±0.3)* | 50(±2)* | 12(±2)* | 3(±1)* | 5(±2)* | $5.7 \times 10^{-2}$ | $8.0 \times 10^{-4}$ |
| | 150 | 88(±3) | 1(±0.3) | 44(±2) | 28(±0.2) | 4(±1) | 11(±7) | $1.7 \times 10^{-2}$ | $4.1 \times 10^{-4}$ |
| LaPO | 90 | 10(±7)* | 0.5(±0.1)* | 5(±3)* | 2(±1)* | 1(±1)* | 1(±1)* | $3.7 \times 10^{-3}$ | $4.9 \times 10^{-4}$ |
| | 110 | 14(±3)* | 1(±0.5)* | 9(±2)* | 1(±0.5)* | 0(±0.5)* | 2(±2)* | $5.7 \times 10^{-3}$ | $6.7 \times 10^{-4}$ |
| | 130 | 32(±6)* | 2(±0.7)* | 17(±0.5)* | 2(±0.6)* | 1(±1)* | 9(±4)* | $1.6 \times 10^{-2}$ | $1.2 \times 10^{-3}$ |
| | 150 | 64(±6)* | 2(±0.3)* | 25(±3)* | 4(±1)* | 4(±1)* | 27(±4)* | $6.0 \times 10^{-2}$ | $1.3 \times 10^{-3}$ |

[a]Reaction parameters: 200 mg catalyst, 0.2 mL min$^{-1}$ DHA solution flow, [DHA] = 0.4 M, temperature 90−150 °C, pressure 10 bar, 6 h time on stream. DHA = dihydroxyacetone, GLA = glyceraldehyde, PVA = pyruvaldehyde, LA = lactic acid, others = pyruvic acid (PA) and glyceric acid (GA), $k$ = rate constant, $r_a$ = DHA conversion rate. The errors associated with the measurement were calculated based on two repetitions of the same tests; if the repetitions were three, it is indicated by *. If no error is reported, it means that the number was obtained by a single catalytic test.

rate was raised (Figure 5A). LaPO, although not mass-transfer-limited under the standard reaction conditions used here (0.2 mL min$^{-1}$ total flow and 212−90 μm particle size at 150 °C), showed a decline of DHA conversion when the total flow was decreased to 0.1 mL min$^{-1}$. In contrast, NbPO is affected by external mass-transfer limitation to some extent as DHA conversion steadily increased as the flow rate was raised.

To understand all the significant contributions on the observed rate, the external mass-transfer coefficient $k_c$ and the intrinsic rate constant $k_s$ were evaluated for LaPO and NbPO, both assuming a first-order (Table S2) and second-order kinetics (Table 2). The value of $k_s$ was multiplied by the initial concentration of DHA to compare the two constants.

The values reported in Table 2 for the second-order kinetics show that $k_c$ and $k_sC_{a0}$ are of the same order of magnitude for LaPO. Thus, neither external mass transfer nor intrinsic kinetics is completely dominant. When raising the flow rate, the value of $k_c$ increased, and its contribution to $k_{obs}$ diminished. In contrast, NbPO $k_c$ is an order of magnitude lower than $k_sC_{a0}$ at all the flows used, meaning that the contribution of the external mass transfer to $k_{obs}$ is significant. Moreover, $\Delta C_A$ (change of DHA concentration across the boundary layer) is 1 order of magnitude lower than $C_{AB}$ for NbPO (Figure S5A) and LaPO (Figure S5B), whereas for ZrPO (Figure S5C), there are 3 orders of magnitude of difference. These results illustrate that mass-transfer limitations are not negligible but also do not exclusively dominate the kinetics under the present conditions. Thus, an explicit deconvolution of $k_c$ and $k_s$ is required for kinetic analysis. Additionally, it is necessary to point out that because of the low apparent density of NbPO, it is not possible to work in a strictly kinetic regime because a further increase in flow rate would cause the catalyst bed to extend outside the isothermal zone of the oven (Figure S6). The fluctuation of the value of $k_s$, with the addition of Gaussian noise to the experimental data for each catalyst, is reported in Figure S7, whereas the values of $k_s$ and $k_c$ for ZrPO are reported in Table S3.



https://dx.doi.org/10.1021/acscatal.0c03761
ACS Catal. 2020, 10, 11936−11950

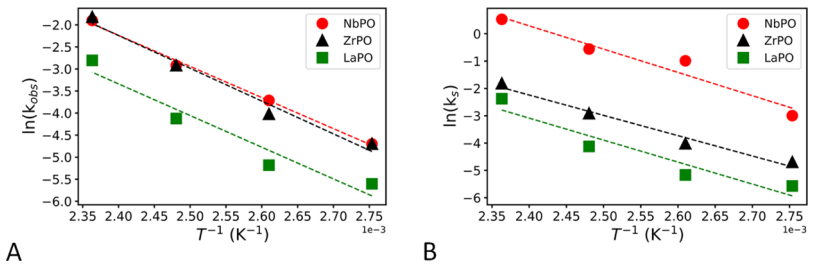


**Figure 6.** Arrhenius plot for LaPO, NbPO, and ZrPO. (A) Based on the observed kinetic rate constant. (B) After removing the contribution of the mass-transfer limitation from NbPO and LaPO.

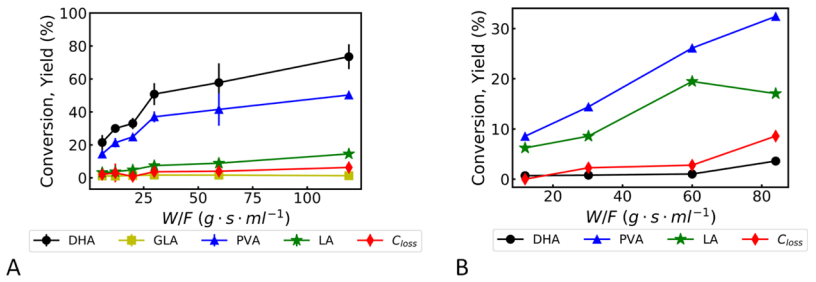


**Figure 7.** Product distribution over ZrPO as a function of $W/F$ ratio, feeding DHA (A) and PVA (B). Reaction conditions: (A) 130 °C, 212−90 $\mu$m particle size, 10 bar, [DHA] = 0.4 M. (B) 130 °C, 212−90 $\mu$m particle size, 10 bar, [PVA] = 0.4 M.

Potential internal mass-transfer limitations were tested, varying the catalyst particle size but maintaining the same reaction conditions. NbPO did not suffer from internal mass-transfer limitations, whereas the DHA conversion over LaPO declined when the largest particle size (425−355 $\mu$m) was used (Figure 5B). However, LaPO was not limited by internal mass transfer under the standard reaction conditions used here (0.2 mL min$^{-1}$ total flow and 212−90 $\mu$m particle size at 150 °C). Finally, it was possible to exclude the internal mass-transfer limitations also for ZrPO as the smallest (75−38 $\mu$m) and the biggest (425−355 $\mu$m) particle sizes showed the same conversion (Figure 5B).

*Kinetics at Different Temperatures.* All the reactions from 90 to 150 °C reached steady state within 2 h, and no measurable deactivation was seen during a 6 h run (Figure S8). NbPO and ZrPO were the most active catalysts, showing 38 and 29% conversion at 90 °C, respectively, whereas LaPO was almost inactive until 130 °C (Table 3). From 90 to 130 °C, the PVA yield over NbPO and ZrPO increased, but it decreased at 150 °C because PVA conversion into LA accelerated. Over LaPO, the PVA yield increased over the whole temperature range, whereas the LA yield was negligible. On the other hand, ZrPO and NbPO reached 28 and 42% LA yield at 150 °C, respectively. The GLA yield was below 1.5% at every temperature for ZrPO and NbPO, whereas LaPO showed an increasing GLA yield with temperature. The carbon loss also increased with increasing temperature. A change in the color of the solution was observed as the temperature increased, moving from transparent at 90 °C to an orange-brown color at 150 °C. A similar color change was reported over SnPO, and it was attributed to the formation of polycondensation products, including humins.[25] The PVA and LA yields increased in the following order: NbPO > ZrPO > LaPO, at each temperature, and these trends are in agreement with the concentrations of Brønsted and Lewis acid sites, respectively. This result was expected as it is well known that Brønsted acid sites are involved in the first dehydration step to produce PVA, whereas sufficiently strong Lewis acid sites are most effective for the Cannizzaro rearrangements of PVA into LA.[82] LaPO, possessing the metal with the biggest ionic radius, is the catalyst with the lowest number of $PO_4$ groups per unit cell and, as a consequence, the lowest density of Brønsted acid sites. On the other hand, the total density of Brønsted acid sites was comparable for NbPO and ZrPO, as was their catalytic performances. LaPO started to show a reasonable conversion of DHA only at high temperatures, probably because this catalyst only contained few Brønsted acid sites, and the Lewis acid sites, which are less active in dehydration reactions, required a higher temperature to start dehydrating DHA.[29,83] It is worth noting that the yield of PVA over LaPO was comparable to the yield of undetected carbon at high temperatures. This observation suggests that a high density of Lewis acid sites without a comparable density of Brønsted ones favors side reactions, such as DHA and/or PVA polycondensation.[45,84]

The apparent activation energies ($E_{a,a}$) for DHA conversion into PVA were 59, 62, and 60 kJ mol$^{-1}$ for NbPO, ZrPO, and LaPO, respectively (Figure 6A). Fully understanding the mass-transfer limitations allowed for the evaluation of the intrinsic kinetic rate constant and the intrinsic activation energy. The intrinsic activation energies ($E_{a,i}$) for NbPO, ZrPO, and LaPO were 71, 62, and 67 kJ mol$^{-1}$, respectively (Figure 6B). The difference between $E_{a,a}$ and $E_{a,i}$ for NbPO supports the fact that this catalyst is only slightly mass-transfer-limited. In fact, the apparent activation energy is usually 10 kJ mol$^{-1}$ or less when a reaction is completely controlled by external mass transfer.[85]

The magnitude of $E_{a,i}$ for the three phosphate catalysts was not very different, suggesting that the catalysts have similar active sites promoting the same kind of chemistry on their surface. Interestingly, the apparent activation energy for LaPO (based on $k_{obs}$) was the lowest, suggesting that the limited conversion over this catalyst was due to an insufficient concentration of Brønsted acid sites. Because strong transport limitations were excluded, this points to the presence of acid sites where the conversion of DHA is sterically hindered. In fact, LaPO is the sole crystalline material in this study.


https://dx.doi.org/10.1021/acscatal.0c03761
ACS Catal. 2020, 10, 11936−11950

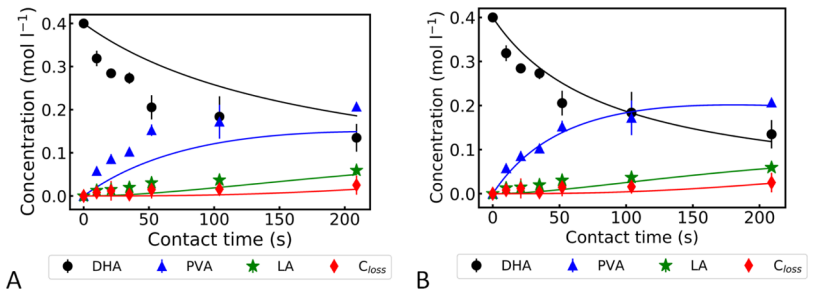


**Figure 8.** Comparison between the experimental results (reported as dots) and the concentration trends obtained using the kinetic rate constant calculated from the reactivity experiments A and calculated fitting the concentration curve with respect to the experimental points B and assuming a second-order reaction for DHA conversion to PVA.

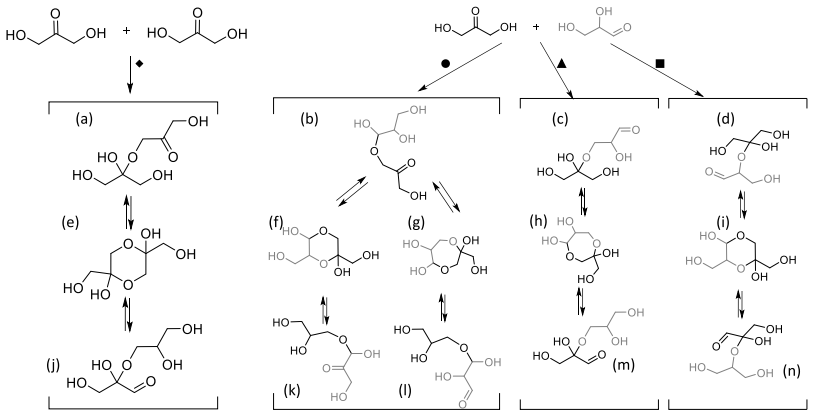


**Figure 9.** Some of the possible dimeric intermediates (a−n) formed from the reaction of two molecules of DHA (♦) or a molecule of DHA with a GLA one (■▲●). The hemiketals/hemiacetals (a−d) could also form five-membered rings not reported in this figure.

*Analysis of Reaction Network.* The formation of different products as a function of $W/F$ was analyzed in detail over ZrPO because this catalyst was not affected by transport limitations (Figure 7A). Similar experiments over NbPO and LaPO are shown in the Supporting Information (Figure S9). As expected, DHA conversion increased from 20 to 70% with increasing contact time, and so did the PVA and LA yields. The carbon loss was lower than 5% at every $W/F$. "Lost carbon" ($C_{loss}$) can be formed by decarbonylation of both LA and PVA and/or the condensation of PVA or DHA to form humins (Figure 1).[86] To deconvolute the contributions from different side reactions, another set of experiments was performed feeding PVA and LA with varying $W/F$.

PVA conversion over ZrPO increased with increasing $W/F$, whereas GLA and DHA yields were negligible at all $W/F$s (Figure 7B). Interestingly, the LA yield increased up to 60 g s mL$^{-1}$, only to then decrease in favor of $C_{loss}$. In fact, the yield of lost carbon increased to 4%, which was in good agreement with the decrease in the LA yield. However, it was not possible to completely reject the participation of PVA in the formation of undetected by-products or deposits. Interestingly, at such high $W/F$s, the DHA yield slightly increased, suggesting that the interconversion of PVA and DHA approaches an equilibrium at high contact times.

To verify the hypothesized reaction network reported in Figure 1, a contact time screening was carried out feeding LA over ZrPO. The chromatograms did not show any peaks other than the LA one even when some conversion was observed at high $W/F$s (Figure S10). These results support the critical role of LA in the formation of undetected products or deposits (lost carbon), but the reaction solution was transparent. In contrast, when PVA or DHA was used as the reactant, the product stream was yellowish. Therefore, it is not possible to exclude the contribution of PVA or DHA to the formation of undetected side products, but it is reasonable to consider their contribution minor compared to that of LA. To gain more insight into the kinetics, the series reaction of DHA to PVA, LA, and by-products was modeled with ODEs (Figures S12−S15). The kinetic constants ($k_1$, $k_2$, and $k_3$) at 130 °C for ZrPO were calculated from the experimental results (feeding DHA, PVA, and LA, respectively) using eqs S1 and S11. Their values, reported in Table S4, were refined through the kinetic modeling. The assumption of a first reaction order for DHA conversion into PVA (Figure S11) was rejected as an apparent second-order reaction better represented the experimental data (Figure 8). The possibility that the apparent second-order behavior is caused by a strong adsorption constant for either PVA or LA was considered. However, we were unable to find a set of chemically reasonable adsorption constants that describe the data using a first-order kinetic model.

In the literature, it is reported that PVA is produced by GLA dehydration.[27] Some authors hypothesized the possibility to produce PVA directly by dehydrating DHA, which is unlikely based on common reactivity trends in organic chemistry.[27] However, none of these possibilities explain an apparent second-order reaction. DHA and GLA are in equilibrium with each other, although DHA seems to be always the most abundant species in solution.[87] Both are likely to form dimers by protecting the aldehydic or ketonic group.[87] The possible hemiketal (or hemiacetal) dimers formed by the reaction of two DHA molecules or by a combination of DHA and GLA are shown in Figure 9. The possible hemiacetals and cyclic


https://dx.doi.org/10.1021/acscatal.0c03761
ACS Catal. 2020, 10, 11936−11950

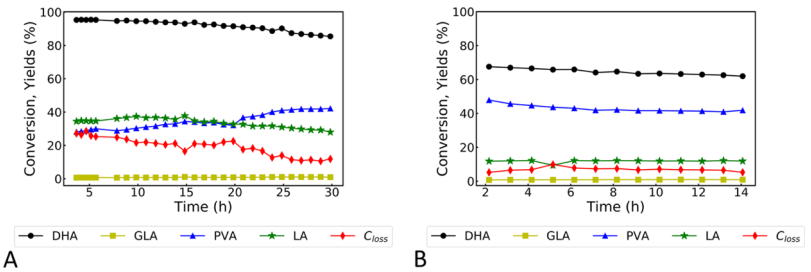


**Figure 10.** Product distribution over NbPO as a function of time on stream. Reaction conditions: (A) 150 °C, 200 mg catalyst, 0.2 mL $min^{-1}$, 425−355 $\mu$m particle size, 10 bar; (B) 130 °C, 200 mg catalyst, 0.2 mL $min^{-1}$, 90−212 $\mu$m, 10 bar.

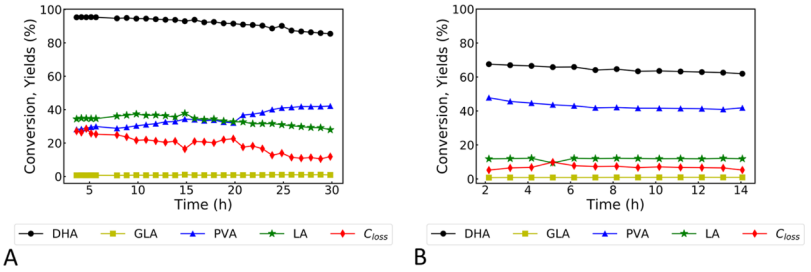


**Figure 11.** Product distribution over ZrPO as a function of time on stream. Reaction conditions: (A) 150 °C, 200 mg catalyst, 0.2 mL $min^{-1}$, 75−38 $\mu$m particle size, 10 bar; (B) 130 °C, 200 mg catalyst, 0.2 mL $min^{-1}$, 75−38 $\mu$m particle size, 10 bar.

intermediates that could be formed from two GLA molecules are reported in Figure S14 as they are less likely to be formed while using DHA as the reactant. It is reasonable to hypothesize that a hemiketal (Figure 9a,c,d) or hemiacetal (Figure 9b) is formed by protecting the C═O moiety of DHA or GLA with an OH of another molecule of DHA or GLA. The hemiketal can successively undergo an intramolecular H-transfer reaction followed by dehydration, releasing a molecule of PVA and GLA (or DHA). Additionally, dimeric intermediates can be involved in humin formation. However, it is not possible to exclude GLA dehydration as a possible reaction pathway. The complete understanding of the reaction mechanism is beyond the scope of the present work, but a full analysis of the interaction between the catalyst surface and DHA or GLA will be the object of a future dedicated study.

*Kinetics of Catalyst Deactivation.* Catalyst deactivation was studied for the two most active catalysts, NbPO and ZrPO. The conversion of DHA over NbPO slowly decreased over time, indicating that the catalyst was deactivating (Figure 10A). The conversion decreased by 2 and 6 percentage points at 150 (from 95 to 92%) and 130 °C (from 68 to 62%), respectively, over the first 15 h on stream. The overall decrease in conversion at 150 °C was 10 percentage points over 30 h (from 95 to 85%). As the analysis of deactivation at a high conversion can be misleading, the evolution of $k_1$ with respect to time on stream is shown in Figure S12 for both temperatures. The rate constant at 150 °C was constant for 6 h and subsequently decreased over time (the decrease is of 71% at 30 h). In contrast, the rate constant at 130 °C decreased steadily over time to lose 21% of its original value after 15 h on stream. The yield of PVA decreased by 10 percentage points within the first 5 h at 130 °C, and it was stable at 40% yield afterward. In contrast, the yields of the other products were not affected by the deactivation within 15 h (Figure 10B). The product distribution observed at 150 °C (Figure 10A) was more interesting. The LA yield was the highest after 15 h, before it started to decrease. PVA showed the opposite behavior. This observation suggests a selective, slow deactivation of the Lewis acid sites necessary to convert PVA into LA, whereas the Brønsted acid sites that convert DHA to LA appear to be deactivated to a lesser extent. The amount of lost carbon decreased with decreasing LA yield. This result suggests that undetected carbonaceous species are mainly formed by the side reactions of LA, possibly by polymerization. These reactions could likely be reduced by diminishing the initial DHA concentration to have more diluted final LA concentration, but this would increase the costs for subsequent separation steps. Thus, further improvements of the catalyst design appear to be necessary.

A similar performance was observed for ZrPO (Figure 11B). DHA conversion decreased by only 8 percentage points over 28 h of reaction at 130 °C. The kinetic rate constant steadily decreased for 20 h and reached an apparent steady state after a 36% reduction (Figure S13B). Interestingly, the conversion was stable around 70% over the first 10 h and around 63% over the last 7 h. The product distribution did not show deactivation over time except for PVA, whose yield decreased by 10% over the first 8 h of reaction. The trend of PVA yield suggests that the concentration of active sites (Brønsted acid sites) is changing over time. The same deactivation trends were observed at 150 °C (Figure 11A). The kinetic reaction rate constant value steadily diminished over 17 h to reach an apparent steady state after a 46% reduction (Figure S13A).

*Characterization of Spent Catalyst.* NbPO showed the most interesting deactivation and, as a consequence, this catalyst was characterized after the reaction. Spent NbPO after 6 and 30 h on stream showed significant weight loss of 10.8 and 24.5% during the temperature-programmed oxidation up to 420 °C (Figure S15). The sample after 6 h showed three well-defined maxima at 47, 299, and 406 °C, whereas the sample after 30 h of reaction showed a fourth peak at 123 °C. The high-temperature peaks are related to the decomposition of macromolecules on the catalyst surface, such as PLA and/or humins. In contrast, the lowest temperature can be related to water desorption. The macromolecules can be formed by polycondensation of PVA, DHA, GLA, or LA.


https://dx.doi.org/10.1021/acscatal.0c03761
ACS Catal. 2020, 10, 11936−11950

The kind of carbon deposited on the catalyst surface after the reaction was characterized by cross-polarized $^{13}$C-MAS-NMR and ATR−FTIR spectroscopy. The solid-state NMR spectrum (Figure 12) showed four peaks in the chemical shift

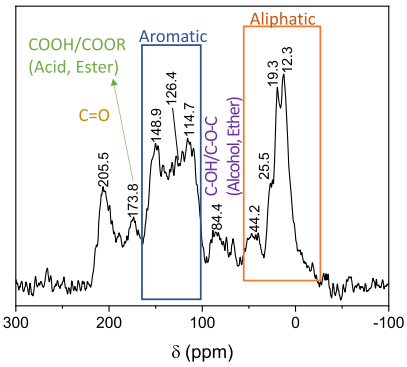


**Figure 12.** $^{13}$C-MAS-NMR spectrum of NbPO after 30 h of reaction.

region of aliphatic carbons (12.3, 19.3, 25.5, and 44.2 ppm, $sp^3$ carbon), many convoluted peaks in the aromatic region (148.9, 126.4, and 114.7 ppm, $sp^2$ carbon), and three more peaks at 205.5, 173.8, and 84.4 ppm related to ketone, acids or esters, and alcohol or ether moieties, respectively.[88] The intensity of this spectrum is low because the sample was not isotopically enriched. Despite the low intensity, the spectrum is quite similar to the one reported by Weckhuysen and co-workers for enriched humins derived by the alkali or acid treatment of sugars (glucose, fructose, and xylose).[89,90] The aromatic peaks detected could be related with the presence of either furan- or benzene-derivatives.[91] Additionally, the intensity in the aromatic region was comparable to the intensity in ketone/aldehyde region, while it was slightly less intense than the aliphatic region. Even though cross-polarization NMR spectroscopy is not quantitative, this suggests that the residual carbon had a diverse chemical makeup. Moreover, the peaks at 173.8 (−C═O), 84.4 (−CH−), and 19.3 ppm ($-CH_3$) ppm can be tentatively related to PLA, whose peaks are at 170, 70, and 17 ppm in its crystalline form.[92] The peak at 84.4 ppm was quite broad, and it can be a convolution of more than one peak, explaining the large shift observed relative to the chemical shift for crystalline LA. This peak was completely absent in the humin spectra reported by Weckhuysen and co-workers.[89−91]

The infrared spectra of the spent catalysts provided similar results (Figure 13). The very crowded C−H deformation region between 1500 and 1300 $cm^{-1}$ could be related to the fingerprint of the aromatic rings or with the CH, $CH_3$ deformation vibration of PLA.[90,93,94] The presence of furans was supported by the peak at 1616 $cm^{-1}$ related to its C═C.[91] The quite intense peak at 1709 $cm^{-1}$ confirmed the presence of C═O as ketonic or aldehydic moieties.[89−91] Furthermore, the shoulder at 1749 $cm^{-1}$ is in strong agreement with the strong C═O of PLA. The shoulder at 1569 $cm^{-1}$ is assigned to the C═C stretching vibration of an alkene.

Not unexpectedly, the characterization of the carbonaceous deposits showed that the kinetic model involving the loss of carbon through a single first-order reaction is simplistic. In fact, the amounts of lost carbon and LA acid concentrations are well modeled only at high contact times (at which the LA concentration is high). It is reasonable that at a low concentration of LA, side reactions of PVA or/and DHA are

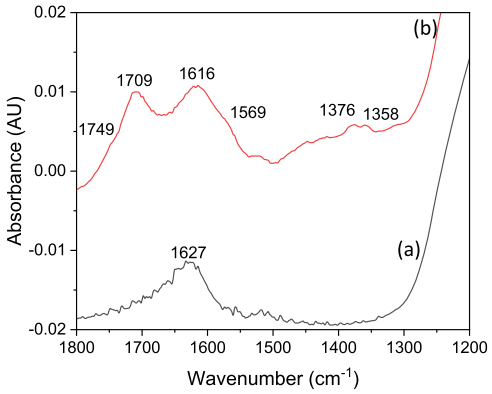


**Figure 13.** ATR−FTIR spectra of fresh NbPO (a) and NbPO after 30 h of reaction (b).

the main contributors to the formation of undetected carbon species. In the literature, it is reported that PVA and DHA can produce solid insoluble humins (∼45%) and soluble polymers (∼10%) by hydrothermal treatment at 220 °C.[86] Additionally, in the presence of an acidic catalyst, LA can undergo dehydration polycondensation.[95,96] The carbon deposits found on the NbPO surface appear to be derived from the polycondensation reaction of DHA, PVA, and LA, which can form the aromatic structures (furanic) by acetal cyclization followed by dehydration.[86] The deactivation of the active sites responsible for LA formation shown in the left-hand side graph of Figure 10 is not surprising. In fact, Lewis acid sites are reported to be active in condensation reactions in the absence of a base.[84,97,98] Therefore, it is likely that the macromolecules detected by NMR and ATR IR spectroscopy are slowly growing and covering the Lewis acid sites responsible for LA production. This hypothesis explains the decrease in the LA yield detected over 30 h and reported in Figure 10.

## CONCLUSIONS

The continuous aqueous phase conversion of DHA into LA is studied using NbPO, LaPO, and ZrPO as catalysts. NbPO is the most active catalyst, although mass-transfer-limited, reaching a LA yield of 36 and 90% DHA conversion at 150 °C. ZrPO shows a lower LA yield (28%), whereas LaPO requires long contact times even to be active toward DHA dehydration. LaPO shows the lowest total concentration of Brønsted acid sites, whereas NbPO and ZrPO show a concentration of Brønsted acid sites 3 times higher than LaPO. Additionally, LaPO possessed only very strong Lewis acid sites. A combination of strong and very strong Brønsted acid sites seems to better assist the dehydration of DHA. NbPO also shows a higher yield of LA than ZrPO, suggesting that sufficiently strong Lewis acid sites are required for the Cannizzaro reaction.

The transport limitations for these catalysts are studied in detail. NbPO and LaPO experience external mass-transfer limitations to a certain extent, whereas ZrPO is completely free from mass-transfer limitation. Based on experiments at different flow rates, the rate constants of mass transfer and the surface reaction are deconvoluted and found to be within 2 orders of magnitude for NbPO and LaPO. An analysis of the reaction products after different contact times shows that DHA is converted to PVA in a second-order reaction, indicating a reaction path *via* dimeric intermediates, which explains why


https://dx.doi.org/10.1021/acscatal.0c03761
ACS Catal. 2020, 10, 11936−11950

DHA does not have to isomerize to GLA, as one would expect based on conventional organic reaction paths.

During a continuous reaction at 150 °C, NbPO slowly deactivates over 30 h of time on stream. Distinct trends are observed for the deactivation of different sites in this bifunctional catalyst. Specifically, the deactivation is more pronounced for Lewis acid sites that are responsible for the conversion of PVA to LA than for Brønsted acid sites that most strongly contribute to DHA conversion to PVA. In fact, the Lewis acid sites also catalyze the polycondensation reactions (of LA, PVA, or/and DHA), which appear to be responsible for the formation of macromolecules on the catalyst surface. These macromolecules are shown to contain domains that are similar to humins and polycondensation polymers like PLA.

## ■ ASSOCIATED CONTENT

### Supporting Information

The Supporting Information is available free of charge at https://pubs.acs.org/doi/10.1021/acscatal.0c03761.

Methods for calculating the activation energy, evaluating the mass transfer and the kinetic model; quantification of sample impurities by PIXE analysis; $N_2$ physisorption curves; MAS-NMR peak deconvolution; $NH_3$ desorption profiles; pyridine adsorption infrared spectra; representation of the primary unit cell of LaPO, NbPO, and ZrPO; mass-transfer coefficient and kinetic constant values for first- and second-order kinetics; graphical representation of the mass-transfer effect deconvolution; oven temperature profile; statistical error of $k_s$; product distribution for the three catalysts with respect to the time on stream (6 h); product distribution for NbPO and LaPO as a function of $W/F$; LA conversion over ZrPO; first-order kinetic fit; values of the kinetic rate constants obtained with the kinetic modeling; decrease of $k_1$ for NbPO and ZrPO with respect to the time on stream at 130 and 150 °C; possible dimeric intermediates formed from the reaction of two molecules of GLA; and TGA profiles of NbPO after reaction (PDF)

## ■ AUTHOR INFORMATION


### Corresponding Author

**Carsten Sievers** − *School of Chemical & Biomolecular Engineering, Georgia Institute of Technology, NW Atlanta, Georgia 30332, United States;* orcid.org/0000-0002-5713-1875; Email: carsten.sievers@chbe.gatech.edu

### Authors

**Giada Innocenti** − *School of Chemical & Biomolecular Engineering, Georgia Institute of Technology, NW Atlanta, Georgia 30332, United States; Dipartimento di Chimica Industriale "Toso-Montanari", Universitá di Bologna, Bologna 40136, Italy; Research Unit of Bologna, Consorzio INSTM, Firenze 50121, Italy;* orcid.org/0000-0003-2951-5457

**Eleni Papadopoulos** − *School of Chemical & Biomolecular Engineering, Georgia Institute of Technology, NW Atlanta, Georgia 30332, United States*

**Giuseppe Fornasari** − *Dipartimento di Chimica Industriale "Toso-Montanari", Universitá di Bologna, Bologna 40136, Italy*

**Fabrizio Cavani** − *Dipartimento di Chimica Industriale "Toso-Montanari", Universitá di Bologna, Bologna 40136, Italy; Research Unit of Bologna, Consorzio INSTM, Firenze 50121, Italy;* orcid.org/0000-0002-4282-6260

**Andrew J. Medford** − *School of Chemical & Biomolecular Engineering, Georgia Institute of Technology, NW Atlanta, Georgia 30332, United States*

Complete contact information is available at: https://pubs.acs.org/10.1021/acscatal.0c03761


### Notes

The authors declare no competing financial interest.

## ■ ACKNOWLEDGMENTS

Financial support from the U.S. National Science Foundation (grant number: CBET-1705444) is gratefully acknowledged. Qandeel Almas and Michael Stellato are acknowledged for collecting the $NH_3$-TPD profiles and the $^{31}P$ MAS-NMR spectra, respectively. Ben Comer and Adam Yonge are acknowledged for the help in debugging some of the Python scripts written to produce part of these data and images. Dr. Marco Fraga and Prof. Will Medlin are acknowledged for the fruitful discussions.

## ■ REFERENCES


(1) Botero, C. D.; Restrepo, D. L.; Cardona, C. A. A Comprehensive Review on the Implementation of the Biorefinery Concept in Biodiesel Production Plants. *Biofuel Res. J.* **2017**, *4*, 691−703.

(2) Lee, R. A.; Lavoie, J.-M. From First- to Third-Generation Biofuels: Challenges of Producing a Commodity from a Biomass of Increasing Complexity. *Anim. Front.* **2013**, *3*, 6−11.

(3) Ajanovic, A.; Haas, R. On the Future Prospects and Limits of Biofuels in Brazil, the US and EU. *Appl. Energy* **2014**, *135*, 730−737.

(4) Bateni, H.; Saraeian, A.; Able, C. A Comprehensive Review on Biodiesel Purification and Upgrading. *Biofuel Res. J.* **2017**, *4*, 668−690.

(5) Katryniok, B.; Kimura, H.; Skrzyńska, E.; Girardon, J.-S.; Fongarland, P.; Capron, M.; Ducoulombier, R.; Mimura, N.; Paul, S.; Dumeignil, F. Selective Catalytic Oxidation of Glycerol: Perspectives for High Value Chemicals. *Green Chem.* **2011**, *13*, 1960.

(6) Bagnato, G.; Iulianelli, A.; Sanna, A.; Basile, A. Glycerol Production and Transformation: A Critical Review with Particular Emphasis on Glycerol Reforming Reaction for Producing Hydrogen in Conventional and Membrane Reactors. *Membranes* **2017**, *7*, 17.

(7) Razali, N.; Abdullah, A. Z. Production of Lactic Acid from Glycerol via Chemical Conversion Using Solid Catalyst: A Review. *Appl. Catal., A* **2017**, *543*, 234−246.

(8) Hill, R. G. Biomedical Polymers. *Biomaterials, Artificial Organs and Tissue Engineering*; Woodhead Publishing, 2005; pp 97−106.

(9) Sinclair, R. G. The Case for Polylactic Acid as a Commodity Packaging Plastic. *Biomater., Artif. Organs Tissue Eng.* **1996**, *33*, 585−597.

(10) Drumright, R. E.; Gruber, P. R.; Henton, D. E. Polylactic Acid Technology. *Adv. Mater.* **2000**, *12*, 1841−1846.

(11) Sin, L. T.; Rahmat, A. R.; Rahman, W. A. W. A. Applications of Poly(Lactic Acid). In *Handbook of Biopolymers and Biodegradable Plastics*; Ebnesajjad, S., Ed.; Elsevier, 2013; pp 55−69.

(12) Castillo Martinez, F. A.; Balciunas, E. M.; Salgado, J. M.; Domínguez González, J. M.; Converti, A.; Oliveira, R. P. d. S. Lactic Acid Properties, Applications and Production: A Review. *Trends Food Sci. Technol.* **2013**, *30*, 70−83.

(13) MarketsandMarkets. *Lactic Acid Market by Application (Biodegradable Polymer, Food & Beverage, Personal Care & Pharmaceutical) & Polylactic Acid Market by Application (Packaging, Agriculture, Automobile, Electronics, Textile), & by Geography Global Trends & Forecasts to 20*, 2015.

(14) Mäki-Arvela, P.; Simakova, I. L.; Salmi, T.; Murzin, D. Y. Production of Lactic Acid/Lactates from Biomass and Their Catalytic Transformations to Commodities. *Chem. Rev.* **2014**, *114*, 1909−1971.

(15) Hara, M.; Nakajima, K.; Kamata, K. Recent Progress in the Development of Solid Catalysts for Biomass Conversion into High Value-Added Chemicals. *Sci. Technol. Adv. Mater.* **2015**, *16*, 034903.
(16) Dapsens, P. Y.; Menart, M. J.; Mondelli, C.; Pérez-Ramírez, J. Production of Bio-Derived Ethyl Lactate on GaUSY Zeolites Prepared by Post-Synthetic Galliation. *Green Chem.* **2014**, *16*, 589−593.
(17) Feliczak-Guzik, A.; Sprynskyy, M.; Nowak, I.; Buszewski, B. Catalytic Isomerization of Dihydroxyacetone to Lactic Acid and Alkyl Lactates over Hierarchical Zeolites Containing Tin. *Catalysts* **2018**, *8*, 31.
(18) Lux, S. Catalytic Conversion of Dihydroxyacetone to Lactic Acid with Brønsted Acids and Multivalent Metal Ions. *Chem. Biochem. Eng. Q.* **2016**, *29*, 575−585.
(19) de Clippel, F.; Dusselier, M.; Van Rompaey, R.; Vanelderen, P.; Dijkmans, J.; Makshina, E.; Giebeler, L.; Baron, G. V.; Denayer, J. F. M.; Pescarmona, P. P.; Jacobs, P. A.; Sels, B. F. Fast and Selective Sugar Conversion to Alkyl Lactate and Lactic Acid with Bifunctional Carbon−Silica Catalysts. *J. Am. Chem. Soc.* **2012**, *134*, 10089−10101.
(20) Nakajima, K.; Hirata, J.; Kim, M.; Gupta, N. K.; Murayama, T.; Yoshida, A.; Hiyoshi, N.; Fukuoka, A.; Ueda, W. Facile Formation of Lactic Acid from a Triose Sugar in Water over Niobium Oxide with a Deformed Orthorhombic Phase. *ACS Catal.* **2018**, *8*, 283−290.
(21) Weber, A. L. Prebiotic Sugar Synthesis: Hexose and Hydroxy Acid Synthesis from Glyceraldehyde Catalyzed by Iron(III) Hydroxide Oxide. *J. Mol. Evol.* **1992**, *35*, 1−6.
(22) Hayashi, Y.; Sasaki, Y. Tin-Catalyzed Conversion of Trioses to Alkyl Lactates in Alcohol Solution. *Chem. Commun.* **2005**, 2716−2718.
(23) Jolimaitre, E.; Delcroix, D.; Essayem, N.; Pinel, C.; Besson, M. Dihydroxyacetone Conversion into Lactic Acid in an Aqueous Medium in the Presence of Metal Salts: Influence of the Ionic Thermodynamic Equilibrium on the Reaction Performance. *Catal. Sci. Technol.* **2018**, *8*, 1349−1356.
(24) Rasrendra, C. B.; Fachri, B. A.; Makertihartha, I. G. B. N.; Adisasmito, S.; Heeres, H. J. Catalytic Conversion of Dihydroxyacetone to Lactic Acid Using Metal Salts in Water. *ChemSusChem* **2011**, *4*, 768−777.
(25) Wang, X.; Liang, F.; Huang, C.; Li, Y.; Chen, B. Highly Active Tin(IV) Phosphate Phase Transfer Catalysts for the Production of Lactic Acid from Triose Sugars. *Catal. Sci. Technol.* **2015**, *5*, 4410−4421.
(26) Assary, R. S.; Curtiss, L. A. Theoretical Study of 1,2-Hydride Shift Associated with the Isomerization of Glyceraldehyde to Dihydroxy Acetone by Lewis Acid Active Site Models. *J. Phys. Chem. A* **2011**, *115*, 8754−8760.
(27) De Clercq, R.; Dusselier, M.; Sels, B. F. Advances in the Conversion of Short-Chain Carbohydrates: A Mechanistic Insight. In *Reaction Pathways and Mechanisms in Thermocatalytic Biomass Conversion I: Cellulose Structure, Depolymerization and Conversion by Heterogeneous Catalysts*; Schlaf, M., Zhang, Z., Eds.; Springer: Singapore, 2016; pp 27−55.
(28) Ennaert, T.; Van Aelst, J.; Dijkmans, J.; De Clercq, R.; Schutyser, W.; Dusselier, M.; Verboekend, D.; Sels, B. F. Potential and Challenges of Zeolite Chemistry in the Catalytic Conversion of Biomass. *Chem. Soc. Rev.* **2016**, *45*, 584−611.
(29) Santos, K. M. A.; Albuquerque, E. M.; Innocenti, G.; Borges, L. E. P.; Sievers, C.; Fraga, M. A. The Role of Brønsted and Water-Tolerant Lewis Acid Sites in the Cascade Aqueous-Phase Reaction of Triose to Lactic Acid. *ChemCatChem* **2019**, *11*, 3054−3063.
(30) Pescarmona, P. P.; Janssen, K. P. F.; Delaet, C.; Stroobants, C.; Houthoofd, K.; Philippaerts, A.; De Jonghe, C.; Paul, J. S.; Jacobs, P. A.; Sels, B. F. Zeolite-Catalysed Conversion of C3 Sugars to Alkyl Lactates. *Green Chem.* **2010**, *12*, 1083.
(31) Janssen, K. P. F.; Paul, J. S.; Sels, B. F.; Jacobs, P. A. Glyoxylase Biomimics: Zeolite Catalyzed Conversion of Trioses. *Stud. Surf. Sci. Catal.* **2007**, *170*, 1222−1227.
(32) Dapsens, P. Y.; Mondelli, C.; Pérez-Ramírez, J. Highly Selective Lewis Acid Sites in Desilicated MFI Zeolites for Dihydroxyacetone Isomerization to Lactic Acid. *ChemSusChem* **2013**, *6*, 831−839.
(33) Dapsens, P. Y.; Kusema, B. T.; Mondelli, C.; Pérez-Ramírez, J. Gallium-Modified Zeolites for the Selective Conversion of Bio-Based Dihydroxyacetone into C1-C4alkyl Lactates. *J. Mol. Catal. A: Chem.* **2014**, *388*−*389*, 141−147.
(34) Taarning, E.; Saravanamurugan, S.; Spangsberg Holm, M.; Xiong, J.; West, R. M.; Christensen, C. H. Zeolite-Catalyzed Isomerization of Triose Sugars. *ChemSusChem* **2009**, *2*, 625−627.
(35) Yang, X.; Wu, L.; Wang, Z.; Bian, J.; Lu, T.; Zhou, L.; Chen, C.; Xu, J. Conversion of Dihydroxyacetone to Methyl Lactate Catalyzed by Highly Active Hierarchical Sn-USY at Room Temperature. *Catal. Sci. Technol.* **2016**, *6*, 1757−1763.
(36) Cho, H. J.; Dornath, P.; Fan, W. Synthesis of Hierarchical Sn-MFi as Lewis Acid Catalysts for Isomerization of Cellulosic Sugars. *ACS Catal.* **2014**, *4*, 2029−2037.
(37) Feliczak-Guzik, A.; Sprynskyy, M.; Nowak, I.; Jaroniec, M.; Buszewski, B. Application of Novel Hierarchical Niobium-Containing Zeolites for Synthesis of Alkyl Lactate and Lactic Acid. *J. Colloid Interface Sci.* **2018**, *516*, 379−383.
(38) Feliczak-Guzik, A.; Sprynskyy, M.; Nowak, I.; Buszewski, B. Synthesis and Physicochemical Properties of Hierarchical Zeolites Containing Ruthenium Oxide Nanoparticles and Their Application in the Reaction of Dihydroxyacetone Isomerization. *Microporous Mesoporous Mater.* **2020**, *293*, 109787.
(39) Takagaki, A.; Goto, H.; Kikuchi, R.; Oyama, S. T. Silica-Supported Chromia-Titania Catalysts for Selective Formation of Lactic Acid from a Triose in Water. *Appl. Catal., A* **2019**, *570*, 200−208.
(40) Oberhauser, W.; Evangelisti, C.; Caporali, S.; Dal Santo, V.; Bossola, F.; Vizza, F. Ethyl Lactate from Dihydroxyacetone by a Montmorillonite-Supported Pt(II) Diphosphane Complex. *J. Catal.* **2017**, *350*, 133−140.
(41) Mylin, A. M.; Levytska, S. I.; Sharanda, M. E.; Brei, V. V. Selective Conversion of Dihydroxyacetone−Ethanol Mixture into Ethyl Lactate over Amphoteric ZrO2−TiO2 Catalyst. *Catal. Commun.* **2014**, *47*, 36−39.
(42) Pighin, E.; Díez, V. K.; Di Cosimo, J. I. Synthesis of Ethyl Lactate from Triose Sugars on Sn/Al2O3 Catalysts. *Appl. Catal., A* **2016**, *517*, 151−160.
(43) Wang, X.; Song, Y.; Huang, L.; Wang, H.; Huang, C.; Li, C. Tin Modified Nb2O5 as an Efficient Solid Acid Catalyst for the Catalytic Conversion of Triose Sugars to Lactic Acid. *Catal. Sci. Technol.* **2019**, *9*, 1669−1679.
(44) Li, L.; Collard, X.; Bertrand, A.; Sels, B. F.; Pescarmona, P. P.; Aprile, C. Extra-Small Porous Sn-Silicate Nanoparticles as Catalysts for the Synthesis of Lactates. *J. Catal.* **2014**, *314*, 56−65.
(45) Kim, K. D.; Wang, Z.; Jiang, Y.; Hunger, M.; Huang, J. The Cooperative Effect of Lewis and Brønsted Acid Sites on Sn-MCM-41 Catalysts for the Conversion of 1,3-Dihydroxyacetone to Ethyl Lactate. *Green Chem.* **2019**, *21*, 3383−3393.
(46) Zhang, Z.; Zhao, Z. Hydroxyapatite Supported Lewis Acid Catalysts for the Transformation of Trioses in Alcohols. *Chin. J. Catal.* **2011**, *32*, 70−73.
(47) Wang, J.; Masui, Y.; Onaka, M. Conversion of Triose Sugars with Alcohols to Alkyl Lactates Catalyzed by Brønsted Acid Tin Ion-Exchanged Montmorillonite. *Appl. Catal., B* **2011**, *107*, 135−139.
(48) Wang, X.; Liang, F.; Huang, C.; Li, Y.; Chen, B. Siliceous Tin Phosphates as Effective Bifunctional Catalysts for Selective Conversion of Dihydroxyacetone to Lactic Acid. *Catal. Sci. Technol.* **2016**, *6*, 6551−6560.
(49) Petrov, I.; Michalev, T. Synthesis of Zeolite A: A Review.*Scientific Papers of the University of Russia*; 2012; pp 30−35.
(50) Wang, X.; Song, Y.; Huang, C.; Wang, B. Crystalline Niobium Phosphates with Water-Tolerant and Adjustable Lewis Acid Sites for the Production of Lactic Acid from Triose Sugars. *Sustainable Energy Fuels* **2018**, *2*, 1530−1541.
(51) Li, X.; Zhixiang, X.; Hongwei, M.; Jinxing, L.; Fukun, L. A Kind of Method That Carbohydrate Selective Catalysis Conversion Prepares Lactic Acid. CN 107162892 A, 2017.


https://dx.doi.org/10.1021/acscatal.0c03761
*ACS Catal.* 2020, 10, 11936−11950

(52) Okuhara, T. Water-Tolerant Solid Acid Catalysts. *Chem. Rev.* **2002**, *102*, 3641−3666.
(53) Zhang, Y.; Wang, J.; Ren, J.; Liu, X.; Li, X.; Xia, Y.; Lu, G.; Wang, Y. Mesoporous Niobium Phosphate: An Excellent Solid Acid for the Dehydration of Fructose to 5-Hydroxymethylfurfural in Water. *Catal. Sci. Technol.* **2012**, *2*, 2485.
(54) Rao, K. T. V.; Souzanchi, S.; Yuan, Z.; Ray, M. B.; Xu, C. Simple and Green Route for Preparation of Tin Phosphate Catalysts by Solid-State Grinding for Dehydration of Glucose to 5-Hydroxymethylfurfural (HMF). *RSC Adv.* **2017**, *7*, 48501−48511.
(55) Saravanan, K.; Park, K. S.; Jeon, S.; Bae, J. W.; Soo Park, K.; Jeon, S.; Wook Bae, J. Aqueous Phase Synthesis of 5-Hydroxymethylfurfural from Glucose over Large Pore Mesoporous Zirconium Phosphates: Effect of Calcination Temperature. *ACS Omega* **2018**, *3*, 808−820.
(56) Hartman, R. L.; McMullen, J. P.; Jensen, K. F. Deciding Whether to Go with the Flow: Evaluating the Merits of Flow Reactors for Synthesis. *Angew. Chem., Int. Ed.* **2011**, *50*, 7502−7519.
(57) Tanimu, A.; Jaenicke, S.; Alhooshani, K. Heterogeneous Catalysis in Continuous Flow Microreactors: A Review of Methods and Applications. *Chem. Eng. J.* **2017**, *327*, 792−821.
(58) Yue, J. Multiphase Flow Processing in Microreactors Combined with Heterogeneous Catalysis for Efficient and Sustainable Chemical Synthesis. *Catal. Today* **2018**, *308*, 3−19.
(59) Sievers, C.; Noda, Y.; Qi, L.; Albuquerque, E. M.; Rioux, R. M.; Scott, S. L. Phenomena A Ff Ecting Catalytic Reactions at Solid − Liquid Interfaces. *ACS Catal.* **2016**, *6*, 8286−8307.
(60) West, R. M.; Holm, M. S.; Saravanamurugan, S.; Xiong, J.; Beversdorf, Z.; Taarning, E.; Christensen, C. H. Zeolite H-USY for the Production of Lactic Acid and Methyl Lactate from C3-Sugars. *J. Catal.* **2010**, *269*, 122−130.
(61) Sushkevich, V. L.; Ordomsky, V. V.; Ivanova, I. I. Synthesis of Isoprene from Formaldehyde and Isobutene over Phosphate Catalysts. *Appl. Catal., A* **2012**, *441−442*, 21−29.
(62) Kishor Mal, N.; Fujiwara, M. Synthesis of Hexagonal and Cubic Super-Microporous Niobium Phosphates with Anion Exchange Capacity and Catalytic Properties. *Chem. Commun.* **2002**, 2702−2703.
(63) Kamiya, Y.; Sakata, S.; Yoshinaga, Y.; Ohnishi, R.; Okuhara, T. Zirconium Phosphate with a High Surface Area as a Water-Tolerant Solid Acid. *Catal. Lett.* **2004**, *94*, 45−47.
(64) Malmusi, A. *Sustainable Catalytic Processes for the Valorisation of Light Alcohols*; Alma Mater Studiorum-Università di Bologna, 2016.
(65) Brunauer, S.; Emmett, P. H.; Teller, E. Adsorption of Gases in Multimolecular Layers. *J. Am. Chem. Soc.* **1938**, *60*, 309−319.
(66) Barrett, E. P.; Joyner, L. G.; Halenda, P. P. The Determination of Pore Volume and Area Distributions in Porous Substances. I. Computations from Nitrogen Isotherms. *J. Am. Chem. Soc.* **1951**, *73*, 373−380.
(67) Tamura, M.; Shimizu, K.-i.; Satsuma, A. Comprehensive IR Study on Acid/Base Properties of Metal Oxides. *Appl. Catal., A* **2012**, *433−434*, 135−145.
(68) Elemental Analysis Inc. Proton Induced X-ray Emission. http://www.elementalanalysis.com/pixe.html (accessed Oct 21, 2019).
(69) Jastrzębski, W.; Sitarz, M.; Rokita, M.; Bułat, K. Infrared Spectroscopy of Different Phosphates Structures. *Spectrochim. Acta, Part A* **2011**, *79*, 722−727.
(70) Fang, L.; Shi, Q.; Nguyen, J.; Wu, B.; Wang, Z.; Lo, I. M. C. Removal Mechanisms of Phosphate by Lanthanum Hydroxide Nanorods: Investigations Using EXAFS, ATR-FTIR, DFT, and Surface Complexation Modeling Approaches. *Environ. Sci. Technol.* **2017**, *51*, 12377−12384.
(71) Hezel, A.; Ross, S. D. Forbidden Transitions in the Infra-Red Spectra of Tetrahedral Anions—III. Spectra-Structure Correlations in Perchlorates, Sulphates and Phosphates of the Formula MXO4. *Spectrochim. Acta* **1966**, *22*, 1949−1961.
(72) Assaaoudi, H.; Ennaciri, A.; Rulmont, A.; Harcharras, M. Gadolinium Orthophosphate Weinschenkite Type and Phase Change in Rare Earth Orthophosphates. *Phase Transitions* **2000**, *72*, 1−13.
(73) Genoveva, G. R.; Enrique, O. R.; Teresita, R. G. E.; Eduardo, O. R. The Influence of Agitation Speed on the Morphology and Size Particle Synthesis of Zr(HPO4)2 H2O from Mexican Sand. *J. Miner. Mater. Charact. Eng.* **2007**, *06*, 39−51.
(74) Mudrakovskii, I. L.; Shmachkova, V. P.; Kotsarenko, N. S.; Mastikhin, V. M. 31P Nmr Study of I-IV Group Polycrystalline Phosphates. *J. Phys. Chem. Solids* **1986**, *47*, 335−339.
(75) Hudson, M.; Workman, A.; Adams, R. High-Resolution Solid-State 31P and 15N Magic-Angle Spinning Nuclear Magnetic Resonance Studies of Amorphous and Microcrystalline Layered Metal(IV) Hydrogenphosphates. *Solid State Ionics* **1991**, *46*, 159−165.
(76) Zah-Letho, J. J.; Verbaere, A.; Jouanneaux, A.; Taulelle, F.; Piffard, Y.; Tournoux, M. "Nb2-XP3-YO12," a Novel NbV Oxophosphate with Disordered Cation Vacancies in a Sc2(WO4)3-Type Structure. *J. Solid State Chem.* **1995**, *116*, 335−342.
(77) Girard, G.; Vasconcelos, F.; Montagne, L.; Delevoye, L. 31P MAS NMR Spectroscopy with 93Nb Decoupling and DFT Calculations: A Structural Characterization of Defects in a Niobium-Phosphate Phase. *Solid State Nucl. Magn. Reson.* **2017**, *84*, 210−215.
(78) Jehng, J.-M.; Turek, A. M.; Wachs, I. E. Surface Modified Niobium Oxide Catalyst: Synthesis, Characterization, and Catalysis. *Appl. Catal., A* **1992**, *83*, 179−200.
(79) Zaki, M. I.; Hasan, M. A.; Al-Sagheer, F. A.; Pasupulety, L. In Situ FTIR Spectra of Pyridine Adsorbed on SiO2−Al2O3, TiO2, ZrO2 and CeO2: General Considerations for the Identification of Acid Sites on Surfaces of Finely Divided Metal Oxides. *Colloids Surf., A* **2001**, *190*, 261−274.
(80) Busca, G. The Surface Acidity of Solid Oxides and Its Characterization by IR Spectroscopic Methods . An Attempt at Systematization. *Phys. Chem. Chem. Phys.* **1999**, *1*, 723−736.
(81) Davis, M. E.; Davis, R. J. *Fundamentals of Chemical Reaction Engineering*; McGraw-Hill: Boston, MA, 2013.
(82) Albuquerque, E. M.; Borges, L. E. P.; Fraga, M. A.; Sievers, C. Relationship between Acid−Base Properties and the Activity of ZrO2-Based Catalysts for the Cannizzaro Reaction of Pyruvaldehyde to Lactic Acid. *ChemCatChem* **2017**, *9*, 2675−2683.
(83) Nash, C. P.; Ramanathan, A.; Ruddy, D. A.; Behl, M.; Gjersing, E.; Griffin, M.; Zhu, H.; Subramaniam, B.; Schaidle, J. A.; Hensley, J. E. Mixed Alcohol Dehydration over Brønsted and Lewis Acidic Catalysts. *Appl. Catal., A* **2016**, *510*, 110−124.
(84) Su, M.; Li, W.; Zhang, T.; Xin, H.; Li, S.; Fan, W.; Ma, L. Production of Liquid Fuel Intermediates from Furfural via Aldol Condensation over Lewis Acid Zeolite Catalysts. *Catal. Sci. Technol.* **2017**, *7*, 3555−3561.
(85) Fogler, H. S. Diffusion and Reactions. *Elements of Chemical Engineering*; Pearson Education Inc., 2006; pp 813−866.
(86) Shi, N.; Liu, Q.; Ju, R.; He, X.; Zhang, Y.; Tang, S.; Ma, L. Condensation of $\alpha$-Carbonyl Aldehydes Leads to the Formation of Solid Humins during the Hydrothermal Degradation of Carbohydrates. *ACS Omega* **2019**, *4*, 7330−7343.
(87) Yaylayan, V. A.; Harty-Majors, S.; Ismail, A. A. Investigation of DL-Glyceraldehyde-Dihydroxyacetone Interconversion by FTIR Spectroscopy. *Carbohydr. Res.* **1999**, *318*, 20−25.
(88) Clayden, J.; Greeves, N.; Warren, S. G.; Wothers, P. *Organic Chemistry*, 2nd ed.; Oxford University Press: Oxford, 2001.
(89) van Zandvoort, I.; Koers, E. J.; Weingarth, M.; Bruijnincx, P. C. A.; Baldus, M.; Weckhuysen, B. M. Structural Characterization of 13 C-Enriched Humins and Alkali-Treated 13 C Humins by 2D Solid-State NMR. *Green Chem.* **2015**, *17*, 4383−4392.
(90) van Zandvoort, I.; Wang, Y.; Rasrendra, C. B.; van Eck, E. R. H.; Bruijnincx, P. C. A.; Heeres, H. J.; Weckhuysen, B. M. Formation, Molecular Structure, and Morphology of Humins in Biomass Conversion: Influence of Feedstock and Processing Conditions. *ChemSusChem* **2013**, *6*, 1745−1758.
(91) van Zandvoort, I.; van Eck, E. R. H.; de Peinder, P.; Heeres, H. J.; Bruijnincx, P. C. A.; Weckhuysen, B. M. Full, Reactive Solubilization of Humin Byproducts by Alkaline Treatment and


https://dx.doi.org/10.1021/acscatal.0c03761
*ACS Catal.* 2020, 10, 11936−11950

Characterization of the Alkali-Treated Humins Formed. *ACS Sustainable Chem. Eng.* **2015**, *3*, 533−543.
(92) Thakur, K. A. M.; Kean, R. T.; Zupfer, J. M.; Buehler, N. U.; Doscotch, M. A.; Munson, E. J. Solid State 13C CP-MAS NMR Studies of the Crystallinity and Morphology of Poly(l-Lactide). *Macromolecules* **1997**, *29*, 8844−8851.
(93) Tai, H.; Upton, C. E.; White, L. J.; Pini, R.; Storti, G.; Mazzotti, M.; Shakesheff, K. M.; Howdle, S. M. Studies on the Interactions of CO2 with Biodegradable Poly(Dl-Lactic Acid) and Poly(Lactic Acid-Co-Glycolic Acid) Copolymers Using High Pressure ATR-IR and High Pressure Rheology. *Polymer* **2010**, *51*, 1425−1431.
(94) Kang, S.; Hsu, S. L.; Stidham, H. D.; Smith, P. B.; Leugers, M. A.; Yang, X.; Ling Hsu, S.; Stidham, D.; Smith, B.; Anne Leugers, M.; Yang, X. A Spectroscopic Analysis of Poly(Lactic Acid) Structure. *Macromolecules* **2001**, *34*, 4542−4548.
(95) Takasu, A.; Narukawa, Y.; Hirabayashi, T. Direct Dehydration Polycondensation of Lactic Acid Catalyzed by Water-Stable Lewis Acids. *J. Polym. Sci., Part A: Polym. Chem.* **2006**, *44*, 5247−5253.
(96) Mehta, R.; Kumar, V.; Bhunia, H.; Upadhyay, S. N. Synthesis of Poly(Lactic Acid): A Review. *J. Macromol. Sci., Polym. Rev.* **2005**, *45*, 325−349.
(97) Mahrwald, R. Diastereoselection in Lewis-Acid-Mediated Aldol Additions. *Chem. Rev.* **1999**, *99*, 1095−1120.
(98) Hassan, Y.; Klein, R.; Kaye, P. T. Aldol Condensation Reactions Effectively Catalysed by Lewis Acid. *Acta Chem. Iasi* **2017**, *25*, 63−72.


https://dx.doi.org/10.1021/acscatal.0c03761
*ACS Catal.* 2020, 10, 11936−11950